Straight line propagation in radio occultation measurements at Mars

A feasibility study for an alternative calculation of refractivity profiles

Thesis report

Daniele Cini

Delft University of Technology

TU Delft

Straight line propagation in radio occultation measurements at Mars

A feasibility study for an alternative calculation of refractivity profiles

by

Daniele Cini

Student Name	Student Number
Daniele Cini	5144191

Instructor:	Håkan Svedhem
Institution:	Delft University of Technology
Place:	Faculty of Aerospace Engineering, Delft
Project Duration:	November, 2021 - July, 2022

Cover Image: Storm over Lake Garda (personal archive)

TU Delft

Contents

List of Figures

1 Introduction

1.1. Radio occultation: general principles and applications

In planetary sciences, the study of the *atmosphere* (where the word is used here with its broadest meaning, thus including the lower, denser neutral layers and the environment at higher altitudes, where gas is rarefied and ionized) is one of those fields whose importance is impossible to overestimate[1]. Some key scientific features that rely on it include:

- The physical properties of the atmosphere are the driving forces of the large-scale phenomena that we identify as ”climate”, therefore: temperatures range and variation; the presence of a system of clouds and/or suspended particles; the existence in liquid form of certain chemical species and their cycle; winds and planetary wind currents; the energy balance in absorption and reflection of incoming solar radiation; the quantity of ionizing solar radiation that reaches the ground; the stratification of gaseous layers varying with altitude according to their temperature and composition.
- The study of trace components in the atmosphere -for example, methane and its variability on Mars (Formisano et al. 2004, Mumma et al. 2009)- can provide information about phenomena occurring under the surface of the planet.
- Planetary atmospheres are gigantic natural laboratories for the study of the interaction between solar radiation, solar wind, magnetic field (where present) and rarefied gas/plasma.
- The chemical composition of the atmosphere cannot be considered constant on a geological scale, and its *current* composition can be used as a ”starting point” in reconstructing the geological history of the planet.
- A proper understanding of the physical properties of planetary atmospheres is essential to design space missions directed towards the surface of these celestial bodies, as entry and descent are among the most critical phases of such missions.

The study of the atmosphere, depending on the quantity that one wants to measure, encompasses various techniques and instruments. Pressure, temperature and wind speed are easily measurable quantities that can be directly probed; spectrometry allows to measure the composition of different atmospheric species from distance, based on the specific interaction that each chemical species has with light; techniques based on the analysis of radio signals sent return information about the electron content of the ionized layers (Schunk and Nagy 2000). Among the techniques within this last category (which are all *indirect* measurements, i.e. they are all based on the analysis of a signal reaching the instrument after *crossing* or *being reflected* by the gas/plasma), radio occultation is a widespread

[1] Naturally, the next lines apply to those celestial bodies -and we restrict our description to the Solar System only- that possess an atmosphere. Notoriously, terrestrial planets with an atmosphere are Venus, Earth and Mars; the gas giants (Jupiter, Saturn, Uranus and Neptune) do have ”atmospheres”, although the lower boundaries of the gaseous envelope is hard to define; moving to the minor bodies, Saturn’s moon Titan is surrounded by a thick atmosphere (with a surface pressure about 50% higher than on Earth (Harri et al. 2006), while Pluto has a tenuous one (10 μbar at the surface, mostly composed of molecular nitrogen (Gladstone et al. 2016); other trans-Neptunian objects, like Eris and Makemake, appear to not have a significant atmosphere (Sicardy et al. 2011, Ortiz et al. 2012)

and well-known method that has been used for over half a century. The underlying principle of this technique is simple: a planetary atmosphere is not a transparent medium for light at radio frequencies, therefore a radio signal travelling through it ”bends” according to the laws of refraction. By measuring the magnitude of the deflection it is possible to reconstruct the optical properties of the crossed medium and, from them, other physical quantities of the medium itself, such as density, pressure, temperature and, in a ionized environment, the total electron content.

Radio occultation has a long legacy. The first scientific papers describing a method to sound the neutral atmosphere of Earth with radio signals from orbiting satellites were published in the 1960s (Fischbach 1965, Lusignan et al. 1969). Although the theoretical foundation of the technique was well-understood, practical applications were limited by the available infrastructures: at that time, the number of orbiting satellites and receiving ground stations could not allow global coverage, therefore impeding a substantial improvement in the existing atmospheric data (Kursinski et al. 1997). Only the advent of GNSS constellations (with the correlated creation of the IGS[2] network of ground stations) granted a constant, global coverage for occultation measurements, which nowadays are used, among other applications, to validate the IRI (International Reference Ionosphere) model, one of the pillars of precise GPS positioning techniques (Bilitza 2018).
The first relevant scientific application of satellite radio occultation measurements was therefore the study of planetary atmospheres in the Solar System. The deflected signals from early interplanetary probes such as *Mariner*, *Pioneer* and *Voyager* missions allowed to study the atmospheres of Venus (Gunnar Fjeldbo, Arvydas J Kliore, and Eshleman 1971), Jupiter (G. Fjeldbo et al. 1975), Saturn (Arvydas J. Kliore et al. 1980), Titan (G F Lindal et al. 1983), Uranus (Tyler et al. 1986), and Neptune (Gunnar F. Lindal 1992).
The study of Martian atmosphere makes no exception: the first radio occultation measurement at Mars was performed with the signals from *Mariner 4*[3] in 1965 (A. Kliore, Cain, et al. 1965). Over the following decades, different missions returned occultation data at different seasons and locations; to name other examples in chronological order, one could mention the Mariner missions that followed *Mariner 4* (launched between 1969 and 1971 A. Kliore, Gunnar Fjeldbo, et al. 1969, A. J. Kliore et al. 1972), the soviet *Mars* missions (launched between 1971 and 1973, Kolosov et al. 1972), the two *Viking* orbiters (operating in 1976) Gunnar F. Lindal et al. 1979), the long-lasting orbiter *Mars Global Surveyor* (operating from 1999 to 2006, Hinson et al. 1999).
All the aforementioned occultation measurements have been performed between a flying spacecraft and a ground receiver on Earth. In particular, satellite-to-Earth radio occultation measurements have provided insightful information on Martian atmosphere over the last decades. In the last years, however, given the increased number of spacecraft orbiting Mars[4], it became possible to exploit *inter-satellite* occultations (i.e. radio frequency measurements between two orbiters) to sound Martian atmosphere. This technique has various advantages over Earth-based radio occultation measurements, which can be summarized in four main categories (Svedhem 2020, Svedhem et al. 2021):

- **Eliminating the effect of Earth's atmosphere**. All signals from interplanetary missions are collected by Earth-based receivers. This means that the signal travels through the whole thickness of Earth atmosphere at variable angles (depending on the local elevation of the spacecraft at the epoch of measurement). Earth atmosphere increases the noise of the signal and introduces an additional frequency shift.
- **Lower distance**. The distance between the two spacecraft is much smaller than the distance between Mars and Earth, therefore a much higher signal-to-noise ratio can be achieved.
- **More scattered measurements**. In satellite-to-Earth occultations, the spacecraft-Mars-Earth geometry is such that the occultation events always occur not far from the planet terminator; moreover, latitudinal drift is slow and therefore repeated measurements over the same area occur at

[2] IGS (International GNSS Service) is ”a voluntary federation of over 200 self-funding agencies, universities, and research institutions [...] working together to provide the highest precision GPS satellite orbits”, whose purpose is to ”provide free and open access to the highest precision products available for scientific advancement and public benefit” (from IGS website: https://www.igs.org/about/#at-glance)

[3] *Mariner 4* was the first spacecraft to perform a flyby of Mars, on July 15th 1965

[4] To give an idea, at the current date (October 2022) *seven* operational satellites are orbiting around Mars: the American *2001 Mars Odyssey*, *Mars Express*, *Mars Reconnaissance Orbiter* and *MAVEN*, the Russian-European *ExoMars Trace Gas Orbiter*, the UAE's *Emirates Mars Mission* and the Chinese *Tianwen 1*

long time intervals; with mutual occultations (and if the orbital geometry is favorable) measurements can be much more scattered (see fig. 1.1 for reference)

- **Reducing the effect of interplanetary plasma**. The interplanetary plasma effect on the signal travelling between two Mars orbiters is minimal (due to both the short distance between the spacecraft and the larger distance from the Sun) when compared to the larger impact it has for a signal travelling from Mars to Earth

With all these advantages comes a drawback, which mainly arises from the flight attitude of the satellites that until the current date (2022) have performed mutual occultations (the discussion is therefore restricted to the Mars Odyssey - Mars Reconnaissance Orbiter (ODY-MRO) and Mars Express - ExoMars Trace Gas Orbiter (MEX-TGO) pairs). The communication subsystems of these orbiters were not *specifically* designed for inter-satellite communication. In fact, those subsystem were either *relay communication systems* (dedicated to create a radio link with landers/rovers on the surface) or *satellite-to-Earth communication systems* (Ao et al. 2015, Svedhem 2020). The immediate consequence of this is that the UHF antennas (the ones that send and receive the signal for the radio occultation measurement) *are not aligned*, meaning that the off-boresight angle is usually quite large and far from optimal[5]. In other words, the attitude constraints of the communication systems are such that the two satellites UHF antennas are not pointed at each other during the occultation event, therefore decreasing the antenna gain.

The first experiment with mutual occultation was attempted between *Mars Odyssey* and *Mars Reconnaissance Orbiter* in 2007. Results displayed a clear signature of Mars' atmosphere (mostly due to the ionosphere). Inversion methods applied to the observed frequency shift returned peak electron densities and peak ionospheric heights that were consistent with existing empirical models (Ao et al. 2015). These promising results pioneered other scientific observations performed with the same technique. A new campaign for mutual occultation measurements between Mars Express (MEX) and ExoMars Trace Gas orbiter (TGO) started on November 2nd 2020 and is currently carried out by ESA. Figure 1.1 displays the latitude of MEX-TGO occultations as a function of time, showing how they are more scattered and numerous than the satellite-to-Earth occultation events: the benefits of this new technique are evident. Data from this particular campaign and ephemeris from the two spacecraft will be used to run this thesis' simulations and to validate the results.

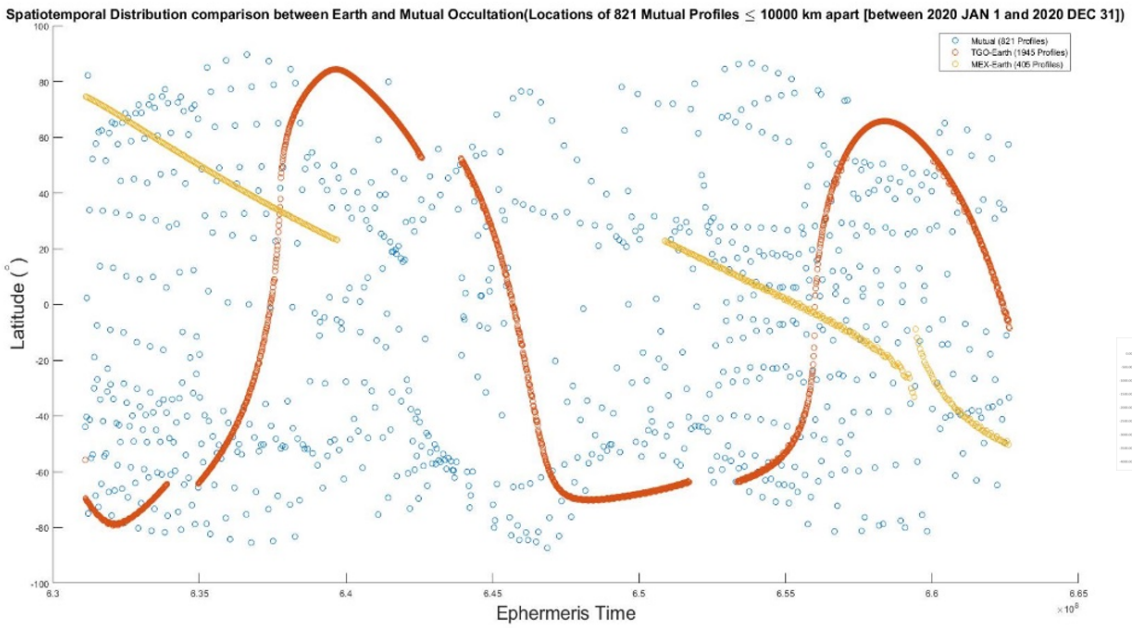

Figure 1.1: Distribution of occultation opportunities for the MEX (*Mars Express*) and TGO (*ExoMars Trace Gas Orbiter*) spacecraft in space and time. MEX-Earth occultations opportunities are marked in **yellow**, TGO-Earth in **orange** and mutual MEX-TGO in **blue** (courtesy of Håkan Svedhem from the conference poster "The MEX–TGO Mutual Radio Occultation Experiment", 2020)

[5] Ao et al. 2015 postulates an angle of 75° as a realistic off-boresight angle in their simulation for the ODY-MRO link budget

1.2. Problem statement: spherical symmetry and "straight line approximation"

When crosslink is established and the receiver measures a frequency (or, more properly, a phase rate) shift, we can identify 4 different causes[6] for it:

1. **Relative motion of the two S/Cs**. This is the dominant cause for the phase rate shift and it corresponds to the well-known *Doppler effect*: a (moving) receiver measures a frequency shift from a (moving) radio source that is proportional to the Δv measured along the line-of-sight.
2. **Ray bending due to refraction**. The presence of a medium induces a change in the ray trajectory[7], thus increasing the nominal ray length by a quantity that depends on the optical properties of the medium crossed and on the mutual geometry medium-ray.
3. **Phase shift in a medium with $n \neq 1$**. Phase is related to wavelength, and the wavelength varies when light travels through a medium.
4. **Relativity effects**. The high speed of the two spacecraft and the proximity to a planetary body suggest that relativity effects may play a non-negligible role.

Coherently with the majority of scientific literature dedicated to radio occultation techniques, relativity effects are not included in this work, as their effect can be estimated with high precision from the knowledge of the orbital geometry and the planetary gravity field (Kursinski et al. 1997). This has an important practical consequence for this work, as it allows classic wave theory to be used. Moreover, it can be proven, thanks to the *calculus of variations* (Melbourne 2004), that point 2. and 3. are in fact two sides of the same phenomenon, and are thus described by the same physical laws.
Therefore, when analyzing the signal, we can ultimately distinguish *two* main sources of phase rate shift: one caused by the relative velocities of the S/Cs -that from now on will be simply referred to as Doppler effect- and one caused by the planetary atmosphere bending the ray (which will be called *atmospheric effect*).

Within the framework of radio occultation measurements, the common assumption is that the atmosphere has a *spherically symmetric structure*: in other words, it is postulated that atmospheric parameters are constant at a given height (in other words, the optical properties are considered to be a function of height only). In this context, spherical symmetry is meant to be a *local* condition: the purely radial dependency is only postulated within the region crossed by the ray path. This assumption has the crucial advantage of simplifying the representation of the atmospheric effect, as *the ray travelling through the atmosphere will be symmetric with respect to the axis passing through the point of maximum curvature*.
This assumption has a much more profound purpose. Spherical symmetry is the necessary condition for *Abel transform* to be applicable. Abel transform is the key mathematical tool in radio occultation techniques, and it has been extensively used to retrieve planetary atmospheric profiles (Gunnar Fjeldbo, Arvydas J Kliore, and Eshleman 1971, G. Fjeldbo et al. 1975, G F Lindal et al. 1983, Gunnar F. Lindal 1992, Kursinski et al. 1997). Spherical symmetry is necessary because it allows to represent the overall atmospheric effect as a function of two parameters only, the *total bending angle* α and the *impact parameter*[8] a -see fig. 1.3 for reference. These parameters can be estimated from frequency measurements: the only additional data required are position and velocity of both spacecraft (to compensate for the Doppler effect). Once α and a are estimated, Abel transform allows to calculate the index of refraction as a function of height from the $\alpha_0, \alpha_1, ..., \alpha_m$ and $a_0, a_1, ..., a_m$ series. A summary of this algorithm can be seen in fig. 1.2).
However, the spherical symmetry hypothesis, though widespread, has obvious limits in terms of adherence to reality: planetary atmospheres *do* have horizontal gradients at a given altitude. For instance, as the rate of ionization depends from the solar zenith angle, a horizontal gradient must exist in the

[6] Signal noise will not be included in the mathematical discussion that follows

[7] In general, the optical properties of the atmosphere vary smoothly, therefore it is expected that the shape of the ray resembles a curve; our simulations will always include differentiable expressions for the index of refraction n, therefore the ray path won't have discontinuities and will always travel in a curved line

[8] This quantity is sometimes referred to in literature as *asymptotic ray miss-distance*; the analogy comes from the field of astrodynamics, where the same name defines the distance between the asymptote of a hyperbolic orbit and the center of the main body. In this case, as the density of the atmosphere thins out until reaching 0, the undisturbed ray would continue its path in a straight line after leaving the atmosphere: a is the distance between the straight line and the center of the planet

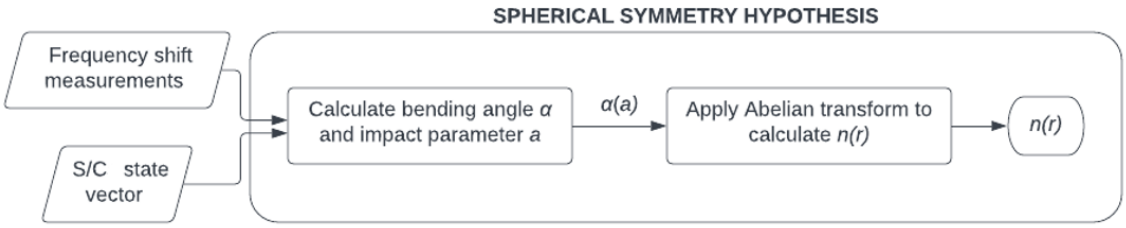

Figure 1.2: Simplified version of the algorithm for calculating n as a function of height under the hypothesis of spherical symmetry

electron density as a function of the position of the Sun over the planet's surface; this effect can be imagined to be even more dramatic at the terminator line.

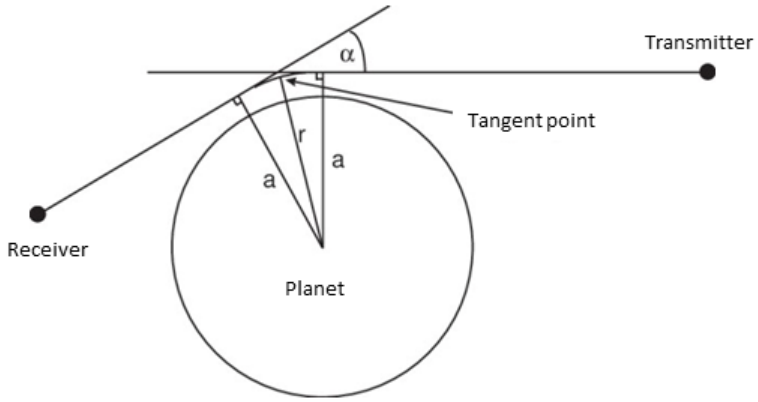

Figure 1.3: Ray path geometry from transmitter to receiver in the plane of propagation for a spherical symmetric medium (figure adapted from Schreiner et al. 1999)

The existence of these asymmetries creates a contradiction. Considering a satellite-to-Earth radio occultations from a spacecraft in Martian orbit: the orbital geometry is such that the occultations happen not far from the terminator line (see fig. 1.4 for reference). In order to use the inversion method based on Abel transform we are forced to adopt the spherical symmetry assumption, but at the same time the occultation happens in one of the regions where horizontal gradients are most likely to be non-negligible. This is a well-known issue and studies performed with radio-occultation measurements on Earth (Shaikh, Notarpietro, and B. Nava 2014) aimed to determine the magnitude of the error introduced by the spherical symmetry assumption. Inter-satellite occultations are not restricted to the terminator region, and their major versatility and less noisy signal (which could carry the traces of horizontal gradients) lead to the question: would it be possible to get rid of the spherical symmetry hypothesis to investigate atmospheric horizontal gradients?
A possible solution comes from the following consideration. The magnitude of the atmospheric effect, in terms of frequency shift, is always much smaller than the typical Doppler effect between two orbiting spacecraft. An examples of this is given in fig. 1.5: on Earth, the maximum atmospheric effect is reached when the ray path crosses the troposphere; in that case, using as a reference the L1 GPS frequency (1575.42 MHz), the maximum effect is between 150 and 200 Hz, while the Doppler shift can reach tens of kHz. Despite being comparatively smaller, the atmospheric signal can be easily detected and it has very visible effects; for the Earth case, refractive bending angles can reach up to 4 deg near the surface (Melbourne 2004). In terrestrial applications (at least, when the ray path is close to the surface), ray bending simply cannot be ignored. On Mars, however, this may not hold true. The planet is smaller, with a less dense neutral atmosphere and a maximum ionospheric electron density that does not exceed 1/10th of Earth's. It is plausible that, for radio occultation measurements at Mars, the estimate of $n(r)$ based on spherical symmetry assumption and Abel transform could be replaced by a *straight line approximation* and *forward propagation*.
By ”straight line approximation” we define an alternate way of defining the Doppler effect. In practice, we *uncouple* point (2) and (3) from the list at the beginning of section 1.2 and we *ignore* point (2); in

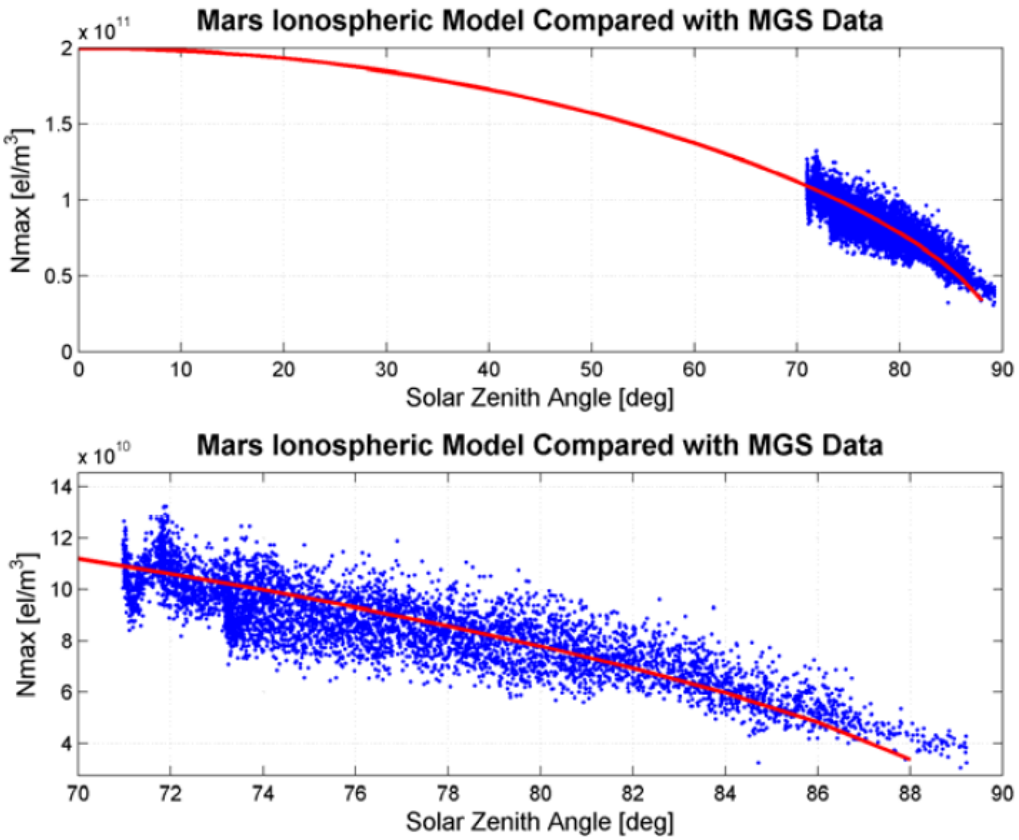

Figure 1.4: Comparison between numerical model and MGS measurements for peak electron density vs solar zenith angle for 5600 profiles derived from the occultation data collected during 1998 through 2005. It is noticeable (especially in the upper panel, where results are extended to solar zenith angles where data are not available) the restricted range of SZA accessible for an orbiter-to-Earth occultation geometry (figure from Pi et al. 2008)

other words, *we assume that the ray trajectory between point A and point B is known in advance, and it is the straight line connecting the two*. The bending induced by the medium (described by Fermat and Snell laws, as it will be shown in section 2.1), is completely ignored.
This assumption has major consequences. The frequency shift measured by a moving observer from a moving source (regardless of the presence of a medium between them) is given by:

$$\Delta f = -\frac{1}{2\pi}\frac{d\phi}{dt} \tag{1.1}$$

where ϕ is the total cumulative phase from point A to point B. Now, if we build a parametric model of the atmosphere in which, for any given point $P(x, y, z)$, it is possible to define the index of refraction n with a certain parametrization:

$$n = \Upsilon(x, y, z, A_1, A_2, ..., A_n) \tag{1.2}$$

then it is possible to calculate the total phase by using the definition of total cumulative phase:

$$\phi = \frac{2\pi}{\lambda}\int_A^B n(x, y, z)ds \tag{1.3}$$

From the cumulative phase, the frequency shift can be approximated via numerical differentiation using eq. (1.1). The advantage given by the straight line approximation procedure is in the estimate of eq. (1.3), because *we know "a priori" the trajectory of the ray (a straight line), therefore we know the path of the integral in eq.* (1.3).
At this point we have a set of of measured frequency shift $\Delta f_1, \Delta f_2, ..., \Delta f_m$ from the occultation event, and a series of frequency shift $\Delta f'_1, \Delta f'_2, ..., \Delta f'_m$ calculated with the straight line propagation and the selected atmospheric parametrization. Through an iterative process of optimization, one can find for

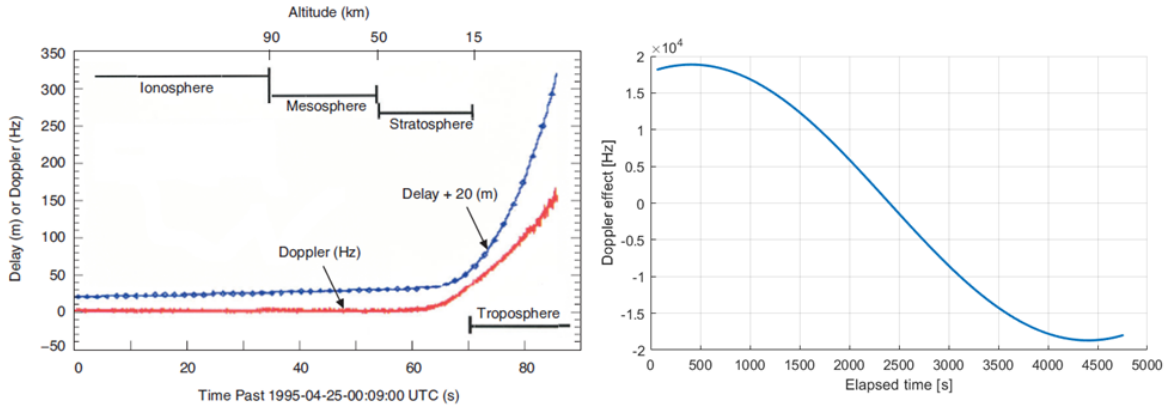

Figure 1.5: Frequency shifts. *On the left:* Profile of excess Doppler (in Hz, red line) and phase delay (in meters, blue dotted line) for a particular occultation event (GPS PRN 28 observed by the GPS/MET experiment on MicroLab-1 on April 25th, 1995) -image taken from Melbourne 2004. The elapsed time of the occultation and the corresponding ray altitude are shown in the horizontal axis. The effect of the troposphere is much larger than any other gas or plasma layer surrounding Earth, and the frequency shift reaches the order of magnitude of 10^2 Hz. *On the right:* Example of Doppler effect for an orbital configuration compatible with the GPS/MicroLab-1 geometry

which set of parameters $A_1, A_2, ..., A_n$ the $\Delta f_i'$ series best approximates the Δf_i measurements. The procedure that has just been described is the ”forward propagation”, which is the second fundamental segment of the new approach proposed. A simplified scheme of the whole algorithm is presented in fig. 1.6. The most immediate advantage of this method is that, while designing the parametrization Υ, spherical symmetry assumption can be abandoned: none of the steps described above requires spherical symmetry to work, therefore it would constitute an unnecessary hypothesis.

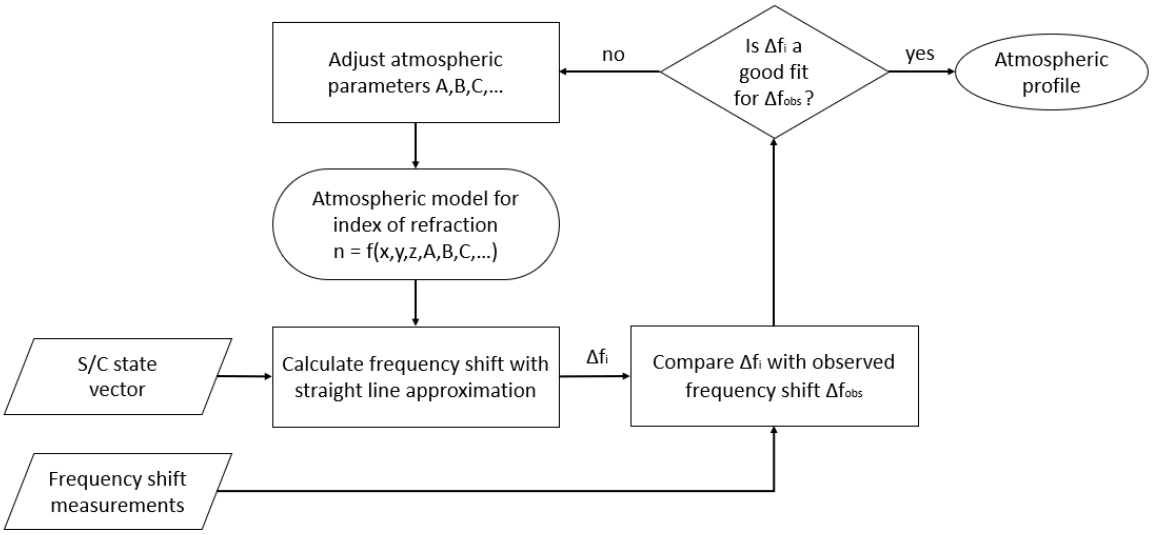

Figure 1.6: Simplified version of the algorithm for calculating atmospheric profiles from the straight-line approximation and forward propagation

In order for this algorithm to be applicable, we must make sure that the error introduced by this approximation (i.e. the ”straight line approximation) stays within an acceptable range; ideally, the best outcome would be to demonstrate that this error is always smaller than the measurement noise in a typical radio-occultation measurement. For the moment the scope of this inquiry will be restricted to mutual occultation scenarios between two orbiters -with a specific focus on the Martian case, but simulations of the Earth case will be performed as well to see whether a thicker atmosphere is a major obstacle for the applicability of the ”straight line approximation”.

1.3. Straight-line approximation in ionospheric tomography

A straight-line approximation for radio signals is commonly put in practice for ionospheric tomography on Earth (Teunissen and Montenbruck 2017). Ionospheric tomography performed with GPS satellites and ground- or space-based receivers exploits the fact that the any GPS satellite transmits *at least* two different signal at different frequencies: this allows to get an estimate of the total electron content (TEC) along the raypath (slant TEC) with a simple linear combination (the *geometry-free* combination, which eliminates all the effects that are not a function of the signal carrier frequency).
We will demonstrate here how this approximation is acceptable. The main goal here is to give an order of magnitude of the quantities involved in the ray bending as it crosses the ionosphere. The total ray *optical length* is given by:

$$L = \int_t^r nds = L_0 + \Delta L \tag{1.4}$$

where L_0 is the distance between transmitter and receiver, while ΔL is the range error (due to ray bending and optical phase delay). This equation can be decomposed as follows:

$$L = \int_{ray} nds = \underbrace{\int_{line} ds_0}_{L_0} + \underbrace{\int_{line} (n-1)ds_0 + \int_{ray} nds - \int_{line} nds_0}_{\Delta L} \tag{1.5}$$

where ds is the infinitesimal path element along the "real" ray and ds_0 is the infinitesimal path element along the straight line connecting receiver and transmitter. In this equation, ΔL contains all the elements related to the presence of the medium in the line-of-sight between transmitter and receiver (as $\int_{line} ds_0$ is just the geometric length of the straight line). ΔL can then be re-arranged as:

$$\Delta L = \underbrace{\int_{line} (n-1)ds_0}_{\propto TEC} + \underbrace{\int_{ray} nds - \int_{line} nds_0}_{\Delta L_{bend}} \tag{1.6}$$

The first term of this last equation is in fact what the straight line approximation: TEC is proportional to a quantity integrated over a straight-line path. To consider this approximation valid, one must demonstrate that the remaining part of the equation, corresponding to ΔL_{bend}, is negligible. An approximate formula is given by (Fehmers 1996):

$$\Delta L_{bend} \approx -\frac{\tan^2 \chi}{8 \cos \chi} X_{max}^2 \tau \left(0.68 - \frac{\tau}{h_t}\right) \tag{1.7}$$

where χ is the zenith angle of the ray at its middle point, X_{max} is the squared ratio of maximum plasma frequency[9], h_t is the height of the transmitter and τ is the ionospheric slab thickness[10]. This number, on Earth, is negligible: table 1.1 shows how the effect of ray bending is much smaller than the one due to the ionospheric phase shift along a straight line (fifth column).

Satellite elevation [°]	Zenith angle [°]	L_0 [m]	ΔL_{trop} [m]	ΔL_{ion} [m]	ΔL_{bend} [m]
90	0	$1100 \cdot 10^3$	2	-1505	0
60	28.1	$1240 \cdot 10^3$	2	-1706	-1
30	54.6	$1100 \cdot 10^3$	5	-2597	-5
10	67.9	$1100 \cdot 10^3$	12	-3999	-25
5	69.6	$1100 \cdot 10^3$	23	-4316	-32
0	70.2	$1100 \cdot 10^3$	100	-4442	-35

Table 1.1: Simulation of tropospheric and ionospheric range errors introduced by ray bending. The transmitting satellite sends a signal with carrier frequency of 150 MHz from an altitude of 1100 km. The ionospheric parameters used are: $N_{e,max} = 2.80 \cdot 10^{12}$ e^-/m^3, $\tau = 300$ km and mean ionospheric height = 400 km

This demonstration suggests that, if the straight line approximation is adequate on Earth for ionospheric tomography, it will likely be valid on Mars (which has a much less denser atmosphere, both in terms

[9] Characteristic quantity of ionospheric plasma, it is proportional to the square root of the electron density
[10] $\tau = TEC/N_{e,max}$

of surface pressure and i terms of electron density) for radio occultation measurements. However, the mathematical domains are different: tomography exploits TEC measurements integrated over lengths, while our proposed method directly uses the frequency shifts measured at the receiver. Therefore, the validity of the straight line approximation must be determined in another way.

1.4. Research objective

This thesis aims to verify whether a straight-line approximation can be used for the study of the atmospheric effect in order to allow for more realistic atmospheric models, based on non-spherical symmetry hypothesis, to be used in future analysis. This will be done by creating a simplified model of the Martian atmosphere (including neutral and charged environment) and performing a simulation of occultation scenarios, after which the frequency residuals from the straight-line approximation and from the curved, ”physically accurate” ray path are compared to calculate the error arising from this approximation; the results will also be compared with real occultation data to validate the simulations and to verify whether the difference between the two approaches is lower than the average signal noise. The main simulation will be accompanied by other simulated scenarios, including mutual occultations around of Earth and in proximity of points with a high horizontal gradient in Mars atmosphere, to serve as comparison for the calculated error.

1.5. Research questions

Based on the research objective, the following research questions can be identified:

- In the context of the study of the atmospheric effect based on residual frequency shift, how large is the difference between straight-line approximation and the ”real” frequency shift?
- How significant is this difference when compared to the measurement noise?
- What are the main differences in the atmospheric effect estimation based on two-satellites occultation events for Mars and Earth?

To answer these questions, this thesis will be structured as follows. Chapter 2 will introduce the different tools needed to simulate an inter-satellite mutual radio occultation event; in particular, there will be a description of: the ray-tracing algorithm, the atmospheric models adopted (both for Mars and Earth), the occultation opportunities (i.e. what geometry defines a favorable occultation event), the real-life instrument that perform the measurement (to adapt the parameters of our simulation to their performance) and the SPICE tool, crucial for simulating orbits of real Martian orbiters. The software created to execute the simulation will be validated and calibrated, and these passages will be shown in chapter 3. Results from the different simulated scenarios will then be shown and interpreted in chapter 4. Finally, chapter 5 contains our conclusions, the answers to the questions stated above and further recommendations for expanding the concept proposed in this thesis.

2

Simulation tools

The purpose of this chapter is to provide an overview of the tools required to run a simulation of an occultation event between MEX (Mars Express) and TGO (ExoMars Trace Gas Orbiter): the numerical methods required to obtain frequency shift profiles, the models for the neutral and charged atmospheric environment, occultation opportunities and spacecraft instrumentation (to adapt the simulation parameters performance to real-life situations) and the available sources of orbital data.

2.1. Ray-tracing for radio signals

The key-point of this thesis is the comparison of the frequency shift resulting from ”real” measurements and from assuming a straight line signal propagation. As we are interested in the *mathematical* difference between these two, we need to design a simulation environment in which the atmosphere, the orbits of the spacecraft and the ray travelling between them are precisely defined. Therefore, even real measurements must be simulated (eventually, real-life measurements from space instruments can be used to *validate* the model).
Before introducing the mathematical tools required for the simulation, a preliminary remark. Throughout this work (as it has been anticipated in chapter 1), we will make use of the *geometrical optics approximation* (in other words, radio signals travelling from transmitter and receiver are described as rays, characterized by quantities such as the *optical path length* and for which a ray path trajectory can be defined). In order for this approximation to be applicable, two conditions must be met (Fehmers 1996):

1. The index of refraction n must not vary significantly over the *first Fresnel zone*[1]
2. Rays must not come close together forming an envelope of tangent lines -in other words, becoming indistinguishable

The second condition, in general, is met in most atmospheric environment: ray envelopes are usually caused by the refraction between different interfaces (generating the phenomenon known as *caustic network*). However, we do have to establish if the first condition is met.
From scientific literature it is known that the ”Fresnel zone condition” is met on Earth (Fehmers 1996), therefore it is reasonable to hypothesize that the same applies on Mars, with a much thinner and rarefied atmosphere. It can be easily verified; the maximum radius of the first Fresnel zone is given by:

$$r_F = \frac{1}{2}\sqrt{d\lambda} \tag{2.1}$$

where d is the distance between the two satellites and λ is the carrier wavelength. The condition is met if the following formula holds true (Fehmers 1996):

$$r_F << \frac{n}{\nabla_\perp n} \tag{2.2}$$

[1] The concept of the Fresnel zone directly descends from the Huygens' principle, according to which any element of a wavefront acts as a secondary wave source - therefore, the advancement of the wave in space can be seen as the result of the superimposition of all the secondary waves. The first Fresnel zone is defined as the volume within which the secondary wavelets emitted in phase are a maximum of π radians out of phase with the wave travelling from transmitter to receiver in the shortest possible path (Fehmers 1996)

where $\nabla_{\perp} n$ is the vertical gradient of the index of refraction. It can be proven that, at ionospheric level, this gradient is proportional to the gradient of electron density (see section 2.2):

$$|\nabla_{\perp} n| \propto \left| \frac{dN_e}{dh} \right| \tag{2.3}$$

If we fill these equations with parameters commonly accepted for Mars ionosphere (see section 2.2) and with the radio frequency used in occultation measurements between MEX and TGO (see next pages) we find that $r_F \approx 1.5 \cdot 10^3$ m, while $n/\nabla_{\perp}(n) \approx 4.7 \cdot 10^6$ m. Condition 1. is met, and geometrical optics approximation can be safely used.

As mentioned above, geometrical optics approximation is useful as it allows us to model the electromagnetic waves in terms of rays, rather than using the more complicated algebra that would derive from using Maxwell equation for electromagnetic waves. As we are describing the radio crosslink between a transmitter and a receiver, our the first concern is to design a method for *ray trajectory determination*: in other words, selecting a proper *ray tracing algorithm*. In our simulation, the ray will travel through Mars ionosphere and through the neutral lower layers. We will focus on the propagation through the ionosphere showing that, given the boundary conditions of this problem, our solution will be equally applicable to the neutral atmosphere.
A vast literature exist for ray tracing in the ionosphere. The first systematic work describing the Hamiltonian equations[2] for the ray path of a radio wave propagating in the Earth's ionosphere (also including the effect of the magnetic field, which leads to a separate description for the ordinary and extraordinary waves[3]) comes from J. Haselgrove 1955; these equations were not solvable analytically so a numerical solution was later developed (C. B. Haselgrove and Jenifer Haselgrove 1960, Jenifer Haselgrove 1963): this set of equations is commonly referred to as the *Haselgrove's equations*. In Bennett, Dyson, and Norman 2004 one can find a comprehensive list of additional hypothesis that have been proposed throughout the years to simplify Haselgrove's equations: in many cases, the effect of Earth's magnetic field is ignored.
One major problem with these equations is that they describe the ray trajectory given a starting point of propagation and an initial direction: they cannot identify the ray path between point A and point B, which has to be found through iterations: the standard approach in this case is be to "shoot" rays in different directions from point A and use their "landing" points (i.e. the closest point to B that the ray reaches) to better estimate the direction for which the ray would end up crossing B, in an iterative process that reaches convergence when the ray passes sufficiently close to B. These methods have been investigated in the past: Reilly 1991 designed a method based on Newton-Raphson algorithm, while Strangeways 2000 applied the Nelder-Mead algorithm to solve the "homing-in" problem. A more recent work (Coleman 2011) developed a point to-point ray tracing method, where all the raypath points between A and B are determined simultaneously; however, this technique requires a first approximation for the raypath, which can be calculated with one of the methods listed in Bennett, Dyson, and Norman 2004.

Ray-tracing has also been performed in scientific works regarding Mars atmosphere. For instance, in Němec, Andrews, et al. 2019, ray-tracing was used to study oblique reflections coming from particular density structures in Martian ionosphere; in that case, the ray-tracing was performed via the Haselgrove's equations (according to the formulation contained in Nickisch 2008). The Martian case can somehow be considered easier to model, because Mars lacks of a significant, structured magnetic field (E. J. Smith et al. 1965, Riedler et al. 1989, Acuña et al. 1998).
It has been reported, however, that localized crustal magnetic fields are at times strong enough to influence both the ionospheric plasma processes and and electron precipitation (Němec, Andrews, et al. 2019). Nevertheless, if we decide to ignore the local and relatively small crustal magnetic field, a much simpler approach towards ray tracing can be identified. As it will be shown in section 2.2, ionospheric

[2] A detailed description of these equations is beyond the scope of this thesis. The basis for Hamiltonian optics is Fermat's principle, which will be introduced later in the text

[3] The geomagnetic field introduces an anisotropy in the plasma environment, which manifests itself as a double refraction that depends on the direction and strength of the magnetic field along the ray path. For the Earth case, the ordinary wave is the left-hand side circularly polarized wave, while the right-hand side polarization corresponds to the extraordinary wave (Teunissen and Montenbruck 2017)

electron density and pressure-over-temperature ratio for the neutral atmosphere define alone, with a good degree of approximation, the index of refraction of the medium. This means that, provided a distribution for the index of refraction n based on a ionospheric and tropospheric model, it could be possible to design an algorithm based on Snell's law only (**eq:snell_law**), excluding the influence of magnetic fields:

$$n_1 \sin\theta_1 = n_2 \sin\theta_2 \tag{2.4}$$

For such a simplified scenario, differential equations for the ray trajectory exist (Born and Wolf 1959):

$$\theta = c \int_{r_0}^{r} \frac{dr}{r\sqrt{n^2 r^2 - c^2}} \tag{2.5}$$

where c is a constant that contains information about the initial ray direction. However, as for Haselgrove's equations, it is rather difficult to provide an *exact* solution for the integral; moreover, this approach does not allow to directly draw a trajectory between two selected points either. Therefore, a ray-tracing method followed by a "homing-in" algorithm must be adopted to describe the raypath through Martian ionosphere.
Different propagators can be designed on the basis of Snell's law. The easiest, most general method consists in propagating the ray and, at regular intervals, considering the refraction happening at the boundary of a hypothetical spherical surface. Faster methods can be implemented on the basis of the *spherical symmetry* hypothesis: Gómez-Correa et al. 2021, for instance, proposed a method based on the *Fermat's ray invariant* (that, for the spherical symmetry, takes the name of *Bouguer's rule* (see fig. 2.1 for reference):

$$rn(\mathbf{r}) \sin\phi = const \tag{2.6}$$

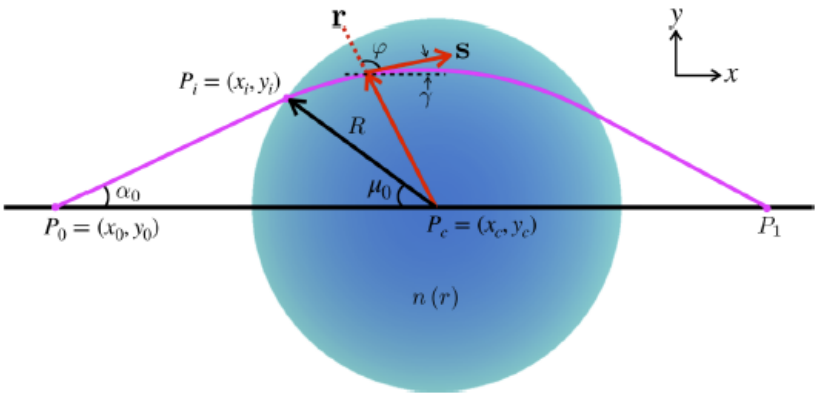

Figure 2.1: The path of rays in a medium with spherical symmetric gradient index (image from Gómez-Correa et al. 2021)

Spherical symmetry, in fact, allows for another substantial simplification: it can be proven that, under spherical symmetry hypothesis, every possible ray is situated in a plane containing the origin (Born and Wolf 1959). However, since we also want to test the "straight line hypothesis" with a non-spherically symmetric atmosphere (to test the goodness of this approximation in highly-asymmetric regions, like the terminator), we are looking for a very general method that can be applicable for all cases (so that the error due to the numerical calculation is always the same).
A good algorithm that appears to have a quite general scope is the one from Sharma, Kumar, and Ghatak 1982 (from now on, the "Sharma method"). The advantage of this algorithm is that it does not require the definition of virtual surfaces to apply Snell's law, nor the knowledge of n *before* and *after* the propagation point (as it is the case of other algorithms, such the one in Zhang et al. 2021); the disadvantage is that it requires the derivative of the index of refraction, which in our case is easily computable (as the atmospheric index of refraction used in the simulation is built on a simple analytical equation, see section 2.2).
The starting point of the Sharma algorithm is the general equation for the ray path in a graded-index

medium (of which Snell's law is a particular case):

$$\frac{d}{ds}\left[n(\boldsymbol{r})\frac{d\boldsymbol{r}}{ds}\right] = \nabla n(\boldsymbol{r}) \tag{2.7}$$

For details we refer to the original paper; the key formulas of the algorithm are:

$$\boldsymbol{R} = \begin{pmatrix} x \\ y \\ z \end{pmatrix} \quad ; \quad \boldsymbol{T} = \begin{pmatrix} T_x \\ T_y \\ T_z \end{pmatrix} = n \begin{pmatrix} \frac{dx}{ds} \\ \frac{dy}{ds} \\ \frac{dz}{ds} \end{pmatrix} \quad ; \quad \boldsymbol{D} = n \begin{pmatrix} \frac{dn}{dx} \\ \frac{dn}{dy} \\ \frac{dn}{dz} \end{pmatrix} = \frac{1}{2} \begin{pmatrix} \frac{dn^2}{dx} \\ \frac{dn^2}{dy} \\ \frac{dn^2}{dz} \end{pmatrix} \tag{2.8}$$

$$\boldsymbol{R}_{n+1} = \boldsymbol{R}_n + \Delta s \left[T_n + \frac{1}{6}(A+2B)\right] \quad ; \quad \boldsymbol{T}_{n+1} = \boldsymbol{T}_n + \frac{1}{6}(A+4B+C) \tag{2.9}$$

$$\begin{aligned} A &= \Delta s \boldsymbol{D}(\boldsymbol{R}_n) \\ B &= \Delta s \boldsymbol{D}\left(\boldsymbol{R}_n + \frac{\Delta s}{2}\boldsymbol{T}_n + \frac{1}{8}\Delta t A\right) \\ C &= \Delta s \boldsymbol{D}\left(\boldsymbol{R}_n + \Delta s \boldsymbol{T}_n + \frac{1}{2}\Delta t B\right) \end{aligned} \tag{2.10}$$

The input for the algorithm are the starting point $\boldsymbol{R}_0$, the initial direction of the ray $\boldsymbol{T}_0$ and an expression for the gradient of the index of refraction ($\boldsymbol{D}$); the output is a list of point coordinates, $\boldsymbol{R}_0$, $\boldsymbol{R}_1$, ..., $\boldsymbol{R}_N$, separated by the same distance Δs.
Once the ray-tracing method is selected, we need to design the "homing-in" algorithm (which, given two points A and B, returns the ray trajectory between them). The hypothesis here is that this ray exists and it is unique (no multipath effect): this assumption will be tested during the simulations.
For its convergence speed, a multi-variable Newton-Raphson method has been selected, similar to the one described in Coleman 2011[4]. We present the general formulas for the three dimensional case:

1. Setting the initial conditions: tolerance ϵ, vector $\boldsymbol{\Delta} = (\Delta x, \Delta y, \Delta z)$, vector $\mathbf{S} = \mathbf{R}_{rec} - \mathbf{R}_{trans}$, initial direction vector $\mathbf{V}_0 = unit(\mathbf{S})$[5]
2. The ray is propagated with the Sharma method until it goes beyond the receiver, i.e. when it crosses the normal line passing through the receiver and perpendicular to the trajectory; in formulas, the stop condition for the propagation is:

   $$[(\boldsymbol{R}_N - \boldsymbol{R}_{rec}) \cdot (\boldsymbol{R}_N - \boldsymbol{R}_{N-1})][(\boldsymbol{R}_{N-1} - \boldsymbol{R}_{rec}) \cdot (\boldsymbol{R}_N - \boldsymbol{R}_{N-1})] < 0 \tag{2.11}$$

   when this condition is met, the last point of the trajectory is defined as the intersection between the segment delimited by $\boldsymbol{R}_N$ and $\boldsymbol{R}_{N-1}$ and the normal line passing through $\boldsymbol{R}_{rec}$. The propagation output are the initial and final direction vectors $\mathbf{V}_0$ and $\mathbf{V}_f$ and the overshoot vector $\mathbf{F} = (F_x, F_y, F_z)$, i.e. the difference between the target point and the last point of the propagated trajectory
3. Point 2. is repeated three times, each time with a different $\mathbf{V}_0$:

   $$\begin{aligned} \mathbf{V}_{0_{\Delta x}} &= unit(\mathbf{S} + (\Delta x, 0, 0) \\ \mathbf{V}_{0_{\Delta y}} &= unit(\mathbf{S} + (0, \Delta y, 0) \\ \mathbf{V}_{0_{\Delta z}} &= unit(\mathbf{S} + (0, 0, \Delta z) \end{aligned} \tag{2.12}$$

   The output are the three overshoot vectors $\mathbf{F}_{\Delta x}$, $\mathbf{F}_{\Delta y}$ and $\mathbf{F}_{\Delta z}$
4. The Jacobian matrix $\mathbf{J}$ is calculated as:

   $$\mathbf{J} = \begin{bmatrix} \frac{F_{\Delta x_x} - F_x}{\Delta x} & \frac{F_{\Delta y_x} - F_x}{\Delta y} & \frac{F_{\Delta z_x} - F_x}{\Delta_z} \\ \frac{F_{\Delta x_y} - F_y}{\Delta x} & \frac{F_{\Delta y_y} - F_y}{\Delta y} & \frac{F_{\Delta z_y} - F_y}{\Delta_z} \\ \frac{F_{\Delta x_z} - F_z}{\Delta x} & \frac{F_{\Delta y_z} - F_z}{\Delta y} & \frac{F_{\Delta z_z} - F_z}{\Delta_z} \end{bmatrix} \tag{2.13}$$

[4]The algorithm has to be tuned to reach convergence, and the coefficients used have been identified through a "trial and error" process, as the work from Coleman 2011 does not contain detailed information about that

[5]The function $unit(\boldsymbol{v})$ is defined as $unit(\boldsymbol{v}) = \boldsymbol{v}/||\boldsymbol{v}||$

5. The new vector $\mathbf{S}'$ is calculated according to the Newton-Raphson equation for k variables and k functions:
$$\mathbf{S}' = \mathbf{S} - \mathbf{J}^{-1}\mathbf{F} \tag{2.14}$$
6. The loop repeats from point 2. with the following conditions:
$$\begin{aligned} \mathbf{\Delta} &= \mathbf{S}' - \mathbf{S} \\ \mathbf{V}_0 &= unit(\mathbf{S}') \\ \mathbf{S} &= \mathbf{S}' \end{aligned} \tag{2.15}$$

Unlike other numerical algorithms such as the bisection method, Newton-Raphson does not necessarily converge to the solution, even if the starting point is not far from the true solution; therefore, the efficacy of this algorithm has to be tested.

As it has been mentioned above, under spherical symmetry hypothesis every possible ray is situated in a plane containing the origin; therefore, as our ray must depart from the transmitter and arrive to the receiver, the plane is the one defined by the two spacecraft and the center of the planet. This simplifies calculations, as can use only two coordinates to propagate the ray; therefore, when spherical symmetry applies, eq. (2.8), eq. (2.9) and eq. (2.10) can be expressed in local x- and y- coordinates only.
As we have one degree of freedom in choosing the two-dimensional reference frame, we select it in such a way that the coordinates of the receiver are $(R_{rec}, 0)$ while the coordinates of transmitter are $(x_{trans}, y_{trans}) = (R_{trans} \cdot \cos\alpha, R_{trans} \cdot \sin\alpha)$ (where α is the angle between transmitter and receiver). The rotation between the two coordinates system is defined by:

$$\begin{aligned} \mathbf{i}' &= \frac{\mathbf{R_{rec}}}{|\mathbf{R_{rec}}|} \\ \mathbf{k}' &= \frac{\mathbf{R_{rec}} \times \mathbf{R_{trans}}}{|\mathbf{R_{rec}} \times \mathbf{R_{trans}}|} \\ \mathbf{j}' &= \mathbf{k}' \times \mathbf{i}' \\ \begin{pmatrix} x_{3D} \\ y_{3D} \\ z_{3D} \end{pmatrix} &= \begin{bmatrix} i'_x & i'_y & i'_z \\ j'_x & j'_y & j'_z \\ k'_x & k'_y & k'_z \end{bmatrix} \begin{pmatrix} x_{2D} \\ y_{2D} \\ 0 \end{pmatrix} \end{aligned} \tag{2.16}$$

In our work, the ray path determination serves the sole purpose of calculating the frequency shift for the two different scenarios, the "real" case (where the ray propagates according to the laws of physics) and the "straight line approximation" case (where the ray, regardless of the medium, propagates in a straight line). For the latter case, the description of the frequency shift is straightforward and comes from classic wave theory (as already mentioned in section 1.2): *the frequency shift measured at the receiver is the derivative of the cumulative phase shift*. In formulas:

$$\Delta f = -\frac{1}{2\pi}\frac{d\phi}{dt} \quad , \quad \phi = \frac{2\pi}{\lambda}\int_A^B n(\mathbf{r})ds \tag{2.17}$$

This means that we can obtain an approximation of Δf by numerically differentiating two consecutive phase estimations.
For the "real" case, eq. (2.17) can be also used, but an analytical solution exists, and the frequency shift between two points moving in a medium can be expressed as (Melbourne 2004):

$$\lambda_0 \Delta f = n_A \mathbf{T}_A \cdot \mathbf{v}_A - n_B \mathbf{T}_B \cdot \mathbf{v}_B \tag{2.18}$$

where $n_{A,B}$ is the index of refraction at point A and B, $\mathbf{T}_{A,B}$ is the initial and final direction vector of the ray and $\mathbf{v}_{A,B}$ are the velocity vectors.
The deep meaning of this formula is worth a closer look. This result comes from an important property of optics, the *stationarity* of ray paths. Stationarity emerges from the *principle of Fermat* (known also as the *principle of the shortest optical path* or the *principle of least time*): it asserts that the optical length $\int_{P_1}^{P_2} nds$ of an actual ray between two points P_1 and P_2 is shorter than the optical length of any other

curve joining these points and lying in a certain regular neighbourhood[6] of it. A weaker formulation of Fermat's principle (which is the one we are interested in) asserts that the actual ray is distinguished from *any* other curve by a *stationary value* of the integral. It can be demonstrated that stationarity leads to another property of ray paths, the *transversality condition*, which prescribes that if one slightly changes the initial and final point of the ray, the phase delay along the new ray minus the phase delay along the old ray depends only on local conditions at the end points. From this, and by using the *calculus of variations*, we can demonstrate that the frequency shift depends only on *local* conditions at the end points and not on the path in between them (Melbourne 2004).
This exact formulation allows to determine the instantaneous frequency shift at epoch t_i; to calculate the contribution of the atmosphere alone, we only need to subtract from the right hand term the value $\dot{r}_{AB}$, i.e. the radial velocity between the end points A and B:

$$\lambda_0 \Delta f_{atm} = n_A \mathbf{T}_A \cdot \mathbf{v}_A - n_B \mathbf{T}_B \cdot \mathbf{v}_B - \dot{r}_{AB} = n_A \mathbf{T}_A \cdot \mathbf{v}_A - n_B \mathbf{T}_B \cdot \mathbf{v}_B - \frac{(\mathbf{v}_A - \mathbf{v}_B) \cdot (\mathbf{r}_A - \mathbf{r}_B)}{|\mathbf{r}_A - \mathbf{r}_B|} \quad (2.19)$$

2.2. Atmospheric models

The refractivity[7] at at a given point inside Mars' atmosphere can be approximated by (Ao et al. 2015):

$$N = 1.306 \frac{p}{T} - 40.309 \cdot 10^6 \frac{n_e}{f^2} \quad (2.20)$$

where p is the pressure (in Pa units), T is the temperature (K), n_e is the electron density (electrons per cubic meter), and f is the radio frequency (Hz).
The first term comes from ideal gas laws and it accounts for the gas mixture in Mars' lower atmosphere. Planetary tropospheres are *non-dispersive media* with respect to the radio waves used in satellite communications, which means that the measured delay is not a function of the carrier frequency. The second coefficient comes from an approximation to the first order of the Appleton-Hartree formula - in particular, for the case in which the radio frequency f is much greater than the plasma frequency (Hargreaves 1992). The charged ionospheric environment is a dispersive medium, as the delay is proportional to $1/f^2$ (frequency-dependent).

As spherical symmetry conditions apply, we are interested in atmospheric profiles that can provide a radial distribution of pressure, temperature and electron density.
For the electron density profile, the model of choice is the so-called *Chapman profile*. Originally created to model Earth's ionosphere, it is based on a manifold of hypothesis: hydrostatic equilibrium, monochromatic incoming radiation, photon-electron single interaction, horizontal atmospheric layers, electrically neutral and homogeneous gas (Chapman 1931). The conditions in which Mars ionosphere exists in a stable way are dissimilar from Earth (as mentioned in the previous section, on Mars there is no magnetic field to form a magnetosphere, and the combined effects of solar wind, chemical reactions and ionization processes are substantially different): therefore, there is no certainty that the Chapman profile would be equally applicable. However, different studies have proved that a Chapman-like function provides an adequate model for Mars' dayside ionosphere (Pi et al. 2008, Sánchez-Cano et al. 2010, Němec, Morgan, et al. 2011, B. Sánchez-Cano et al. 2013).
The general equation for a Chapman profile is:

$$n_e(h, \chi) = N_{e,0} \exp\left[\frac{1}{2}\left(1 - \frac{h - h_{m,0}}{H} - \sec(\chi) \cdot \exp\left(-\frac{h - h_{m,0}}{H}\right)\right)\right] \quad (2.21)$$

where h is the height above spherical planet, χ is the solar-zenith angle and $h_{m,0}$, H are, in order, the height of maximum density and the scale height ($z = \frac{h - h_{m,0}}{H}$ is the reduced height, while $N_{e,0}$ is the maximum electron density at $\chi = 0$ and $h = h_{m,0}$). It is worth mentioning that the simple function $\sec(\chi)$ in eq. (2.21) is a good approximation for SZA dependency only for those regions sufficiently

[6] Where a *regular neighbourhood* is the region covered by rays in such a way that one and only one ray passes through each point of it
[7] Refractivity is proportional to the index of refraction according to the formula $n = N \cdot 10^{-6} + 1$

far away from the terminator line (SZA<75°): beyond this limit, the more complex "Chapman grazing function" (Ch) should be adopted, whose defining expression is:

$$Ch(X,\chi) = X \sin\chi \int_0^{\chi} \frac{\exp\left(X - X\frac{\sin\chi}{\sin\phi}\right)}{\sin^2\phi} d\phi \tag{2.22}$$

where $X = R/H$. This formula will be discussed more in detail section 4.3, where an asymmetric ionosphere is simulated.

The selection of a ionospheric profile is critical for this simulation, as the charged environment is expected to be the major contributor to the signal phase shift (Ao et al. 2015). Our design choice is to build a *worst case scenario* profile, i.e. to identify and choose those conditions that lead to a maximum in the peak electron density. Therefore:

1. The electron density profile at the sub-solar point will be considered representative for the entire surface of Mars
2. If the model contemplates this possibility, it is assumed that Mars is at perihelion
3. If the model contemplates this possibility, it is assumed that the Sun is in a phase of intense solar activity

Point 1. comes from the necessity of selecting a unique profile with the highest electron density -as we must adhere to spherical symmetry assumption. Points 2. and 3. maximize the electron density peak, since a major proximity to the Sun and a higher level of solar activity correspond to a higher rate of ion production in the upper layers of planetary atmospheres.
Different ionospheric profiles are available in dedicated scientific literature: the following list summarizes their main characteristics.

- The profile from Ho, Golshan, and A. Kliore 2002 was included in the NASA Radio Wave Propagation Handbook for Communication on and Around Mars for the year 2022; at the time the only data available came from radio occultation experiments and from the only in-situ ionospheric measurements obtained by two Viking landers.
- The model developed in Pi et al. 2008 is more sophisticated: based on about 5600 occultations during the years 1998-2005 between Earth and Mars Global Surveyor, it includes two different layers (P-layer and S-layer); given the occultation geometry, the sampled SZA are in the range 71°-90° (which is acknowledged to cause deviation from the true value, as it was observed that H decreases with the SZA), and most of the measurements are performed over the Northern hemisphere ; the coefficient $N_{e,0}$, $h_{m,0}$ and H returned are average values over more than a half of a solar cycle.
- In Němec, Morgan, et al. 2011 the function describing the ionospheric density is not entirely a Chapman profile: the curve is divided into three parts, among which only the first one (approximately up to 130 km) is described by a Chapman function; for higher altitudes, a *transition zone* and a *diffusion region* are expressed by sophisticated equations that take into account also the magnetic latitude; formulas describing the key parameters as a function of solar cycle phase and distance from the Sun are given.
- Similarly, B. Sánchez-Cano et al. 2013 created an empirical model, called *NeMars*, for the dayside ionosphere electron density profiles, including a primary and a secondary layer; the model is built on data from Mars Express' MARSIS instrument (and, to a lesser extent, on occultation data from the Mars Global Surveyor mission) and consists of two quasi-Chapman profile (a minor modification on the parameter H is applied); explicit equations for the dependency from Sun distance and solar activity are given.
- Lastly, the profile used in Nava et al. 2020 is a working model to determine the expected shape and magnitude of the frequency shift in mutual occultation measurements; no dependency from season or solar activity is introduced.

All the aforementioned models are displayed in fig. 2.2). In this picture, profiles are taken for SZA=0°; moreover, for those profiles that allow it (Němec, Morgan, et al. 2011, B. Sánchez-Cano et al. 2013) the curve is calculated in the "worst-case scenario" of high solar activity and perihelion.

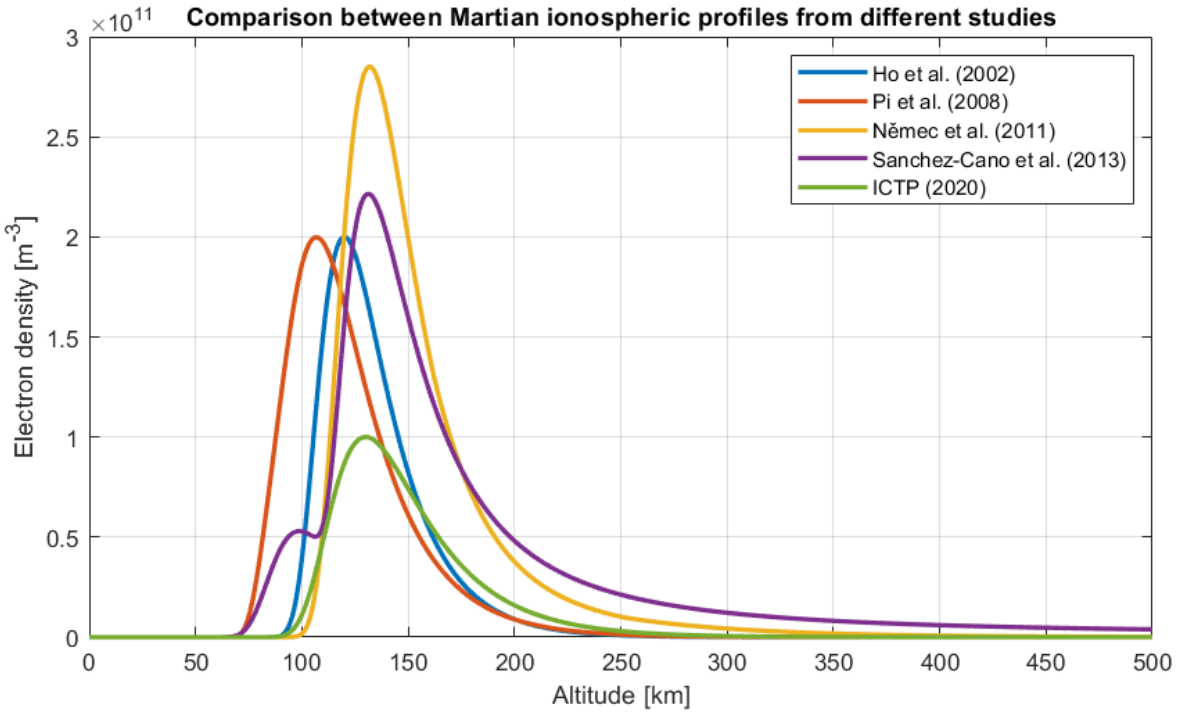

Figure 2.2: Ionospheric profiles retrieved from five different studies. Profile sampled at $\chi = 0°$ and (when possible) in conditions of maximum solar activity and minimum distance from the Sun

The selected model is the one proposed in B. Sánchez-Cano et al. 2013. The choice has been made because in that work the functions used for the density profiles are (quasi-) Chapman functions, therefore easy to represent and to differentiate analytically -an important feature that simplifies the ray-tracing algorithm. Moreover the explicit expressions for the Sun-distance and solar cycle dependency allow to easily represent the worst-case scenario we identified.
However, some minor modifications must be implemented to make this model usable for this work. In order to easily interpret the ray path behavior as a function of altitude it is recommendable that the ionospheric density curve has a clear "bell shape": therefore, we will not include the secondary layer at lower altitudes (clearly visible in fig. 2.2, first maximum of the purple line). Moreover, the equation for the primary layer includes a peculiar representation of the parameter H, which varies with altitude:

$$H = H_0 + m(h - h_0) \tag{2.23}$$

where $H_0 = 2.6 \exp(\chi/100.5) + 9.4$ and $m = 0.08 - 0.00035\chi$. This additional parametrization has been introduced to account for electron density measurements at high altitudes that could not be adequately represented by previous models (such as Němec, Morgan, et al. 2011). However, the resulting Chapman profile does not tend to 0 for $h \to \infty$ as it would be expected from a standard Chapman profile[8], which could create a bias in case the transmitting satellite (in our case, MEX with its highly-elliptical orbit) operates at high altitudes. Therefore, we need to identify a constant value for H that can be representative for the whole profile. The selected method is a simple *numerical least-squares interpolation* for the values between 100 and 450 km, which returns $H = 13.3$ km. The other values for the one layer Chapman profile are $h_{m,0} = 132,4$ km and $N_{e,0} = 2 \cdot 10^{11}$ e^-/m^3

For the first part of eq. (2.20), the issue is to define temperature and pressure profiles that can be representative for the whole planet: atmospheric profiles display a vast range of variation, as a function of

[8] It could be argued that the residual electron density obtained as $h \to \infty$ represents the electron density of the interplanetary medium. However, this hypothesis is wrong for 2 reasons: first, the two values do not coincide, as solar wind electron density at Mars orbit is approximately $4 \cdot 10^6$ e^-/m^3 (Knudsen et al. 2016) whereas $N_{e,\infty} \approx 6.4 \cdot 10^8$ e^-/m^3; second, and most importantly, describing the solar wind density is not in the scope of the Chapman function. A Chapman profile describes the ion production rate of a neutral gas sheet, therefore the electron density should decrease to 0 as atmospheric species disappear with increasing altitude

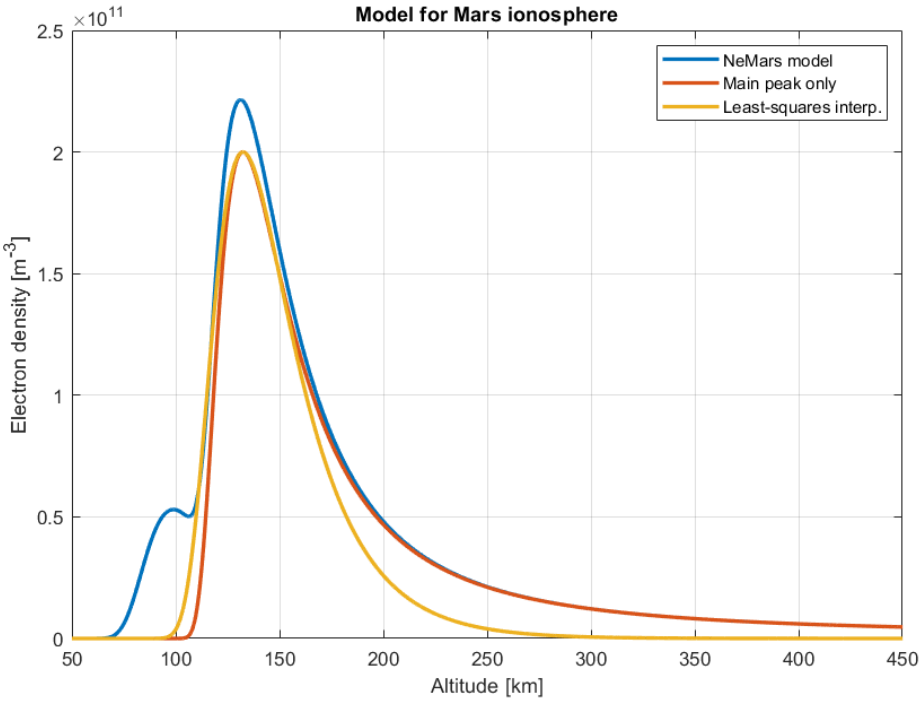

Figure 2.3: The ionospheric profiles derived from NeMars model (B. Sánchez-Cano et al. 2013). In **blue** the NeMars profile, with the clearly distinguishable primary and secondary peaks; in **red** the NeMars profile without the secondary peak; in **yellow** the best-fitting profile

season, latitude, dust conditions and Sun angle (M. D. Smith 2008). The solution adopted for our simulation comes from the work of Ho, Golshan, and A. Kliore 2002, where atmospheric profiles retrieved from Mars Global Surveyor radio occultation experiment[9] were combined with the tropospheric effect formula $N = 1.306p/T$ and the resulting curve was interpolated via a best-fitting exponential function. The resulting expression for the neutral gas contribution to refractivity is:

$$N = N_0 \exp\left(-h/H_N\right) \tag{2.24}$$

where $N_0 = 3.9$ and $H_N = 11.0 \cdot 10^3$ m.

For the Earth case, which serves as a comparison for results on Mars, the complete expression for refractivity is (Kursinski et al. 1997):

$$N = 0.776\frac{p}{T} - 40.309 \cdot 10^6 \frac{n_e}{f^2} + 3.73 \cdot 10^3 \frac{p_w}{T^2} + 1.4 \cdot 10^{-3} W \tag{2.25}$$

where the new terms on the right side account for water vapor (p_w = water vapor partial pressure in Pa) and liquid water (W = liquid water content in kilogram per cubic meter). In our study we will only consider the dry atmosphere case, so the last two terms of the equation will be ignored.
A plethora of profiles for Earth's neutral atmosphere and ionosphere is available in scientific literature. Since we need a standard model for which geographic effects and seasonal variations are levelled out, our preferred choice for the atmospheric model is the open source *U.S. Standard Atmosphere 1976* (United States Committee on Extension to the Standard Atmosphere 1976). The analytical expressions for pressure and temperature, although simple, vary with altitude to account for the stratification of Earth's atmosphere, and this complicates the resulting expression for N. Therefore, the solution is the same one adopted for the Mars case: interpolating the expression $N = 0.776p/T$ to obtain a best-fitting exponential model for refractivity. The solution is an expression identical to eq. (2.24): for Earth, $N_0 = 332.8$ and $H_N = 6.94 \cdot 10^3$ m.

[9] The data were retrieved on January 28th 1998, at coordinates 25.3N and 127.1E, at 05:35am local time in the autumn season

Planet	Ionospheric model	$N_{e,0}$ [e^-/m^3]	h_m [m]	H [m]
Mars	Chapman (spherical symmetry) Chapman (Ch = \sec{\chi}) Chapman (Ch = numerical approximation)	$2.0 \cdot 10^{11}$	$132.4 \cdot 10^3$	$13.3 \cdot 10^3$
Earth	Chapman (spherical symmetry)	$1.0 \cdot 10^{12}$	$350 \cdot 10^3$	$100 \cdot 10^3$

Table 2.1: Models and parameters for Earth and Mars ionospheres

Regarding the ionosphere, Earth's charged environment has been studied in detail for decades with several different methods and measurements (including ionosondes, incoherent scatter radars, rockets, topside sounders and in situ satellites, GNSS radio occultations) and the models available are usually quite sophisticated. They generally differ in purpose: while some models, for instance, are simplified expressions that allow for a first-order estimation of the ionospheric effect in GNSS applications (such as the Klobuchar or the NeQuick-G), others are meant to be a synthesis of all world-spread measurements combined into a comprehensive formulation (it is the case of the International Reference Ionosphere, or IRI) (Teunissen and Montenbruck 2017). Even more complex description can be found in physical models, which are able to return not only electron densities but also the distribution of charged and neutral species in the upper atmosphere: it is the case, to mention a few, of the CTIPe, USU-GAIM, and TIE-GCM models.
For the purpose of this work, we are looking for another Chapman profile that can be representative of the average behavior of the day-side ionosphere. The required coefficients are taken from Hernández-Pajares et al. 2011 and are $N_{e,0} = 1.0 \cdot 10^{12}$ e^-/m^3, $h_0 = 350 \cdot 10^3$ m, $H = 100 \cdot 10^3$ m. A summary of the parameters and the model used for the simulations can be found in table 2.1.

2.3. Occultation opportunities

Two different types of event can be distinguished in radio occultations: *ingress* (when the satellite receiving the signal sees the other satellite disappear below the horizon; ray altitude decreases with time) and *egress* (when the receiving satellite sees the other satellite rising from the horizon; ray altitude increases with time). The mathematical description of these two types of event is the same: they can be considered equivalent, specular events.
Sometimes the geometry of the event can be slightly more complex. The first radio occultation experiment between Mars Odyssey and Mars Reconnaissance Orbiter, for instance, occurred between two satellites in low, quasi-polar Martian orbits, *nearly counterrotating* (MRO has a nominal 3 P.M. ascending node, while ODY has a 5 P.M. descending node). This means that the two satellites come into view of each other two times per orbit (once on each side of the planet) and the event can be described as an egress occultation followed shortly after by an ingress occultation (Ao et al. 2015).
The case of MEX and TGO presents a different peculiarity: at the epoch of the mutual radio occultation campaign, TGO flied in a circular, low Mars orbit (LMO), while MEX had a quasi-polar, highly eccentric orbit. More in detail: ExoMars Trace Gas Orbiter orbits at 400 km of altitude, with an inclination of 74° and a period of ≈ 2 hours[10]; Mars Express has an orbital inclination of 86.9°, apocenter at 10530 km and pericenter at 330 km (thus resulting in a high eccentricity value, $e = 0.571$) and an orbital period of 7 hours[11] (-see fig. 2.5). Therefore, if we define an "occultation opportunity" any event in which the line of sight between transmitter and receiver crosses a portion of the atmosphere (i.e. the line-of-sight crosses altitudes lower than TGO), the result is that there is a large variety of possible configurations for these events.

[10] Source: https://www.eoportal.org/satellite-missions/exomars#tgo-trace-gas-orbiter
[11] Source: https://www.eoportal.org/satellite-missions/mars-express#spacecraft

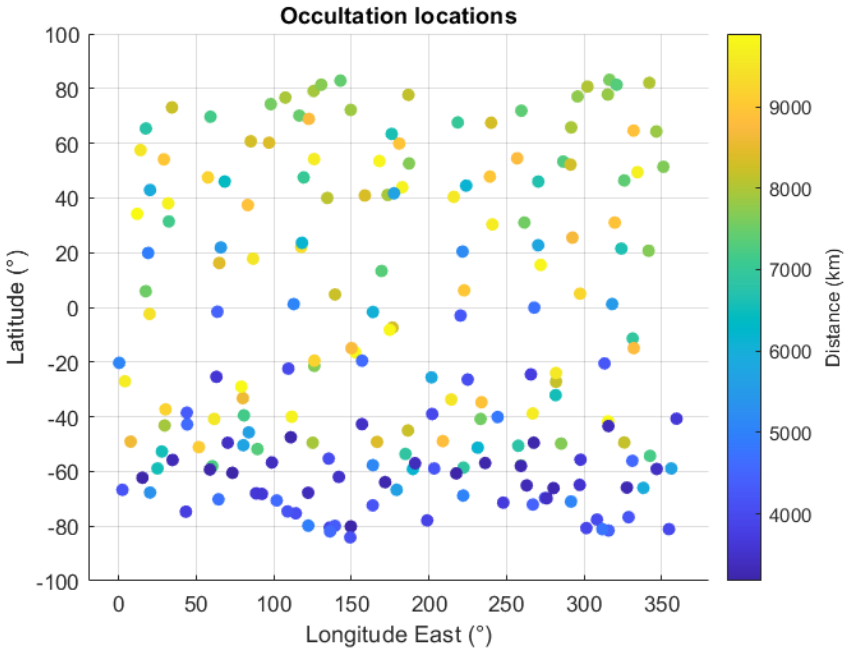

Figure 2.4: Approximate locations for MEX-TGO occultation opportunities between October 16th and November 30th 2020. The color indicates the maximum distance between the two S/Cs throughout the occultation event

A practical consequence of this is shown in fig. 2.4, where the approximate ground plot of 200 different occultation opportunities between October 16th and November 30th 2020 is displayed. The majority of the events (61%) takes place in the southern hemisphere, which also sees on average the shortest distance between the two satellites. This is due to the highly-elliptical geometry of MEX orbit, which at that time had its periares point in proximity of the South Pole.
For our simulation, we will select the event of December 1st 2020 at 18:04:00 Terrestrial Time.

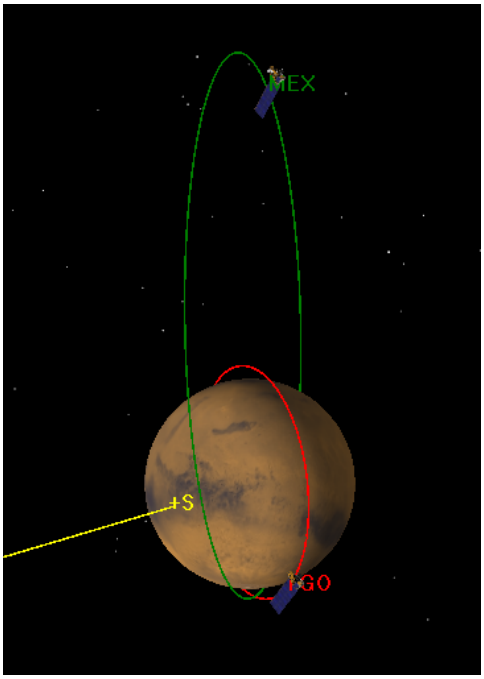

Figure 2.5: Graphic representation for MEX (**green** trajectory) and TGO (**red** trajectory) orbits during November 2020. The "+S" vector indicates the direction of the Sun

2.4. Spacecraft instrumentation

Before using the real data from MEX and TGO it is worth mentioning what kind of instruments have produced those data.
MEX and TGO are both equipped with UHF relay payloads for proximity link communications with landed assets. The need for such subsystem were originally identified for the MEX mission (though they are equally applicable for ExoMars) and include (Edwards et al. 2003):

1. The need to support an increasing scientific data flow from the surface of Mars. The two rovers *Spirit* and *Opportunity* alone were expected to generate large data volumes with their PANCAM instruments, and other lander/rover missions were in sight at the time of MEX design
2. Surface missions must be equipped with energy (and mass) efficient communication systems. Given the high expected density of scientific payload on board landers and rovers, the high energy-per-bit required for direct-to-Earth communications and the operational complexity of pointing a high-gain antenna would be prohibitive
3. Engineering telemetry data during the critical phases of *entry*, *descent* and *landing* are highly valuable, as in case of failure they allow to diagnose what went wrong and to learn from experience for the benefit of future missions: again, these data cannot be transmitted with direct-to-Earth communication links

Mars Express Orbiter is older than ExoMars TGO (the former was launched on June 2nd 2003 for a nominal mission from January 2004 to November 2005, while the latter was launched on March 14th 2016); it carried the first generation of UHF relay payloads, a Melacom transceiver (developed by the UK company QinetiQ). The transponder (operating in the range 401-437 MHz) is connected to two 2 patch antennas for spacecraft-to-surface link with any landed asset that supports the *Proximity-1* protocol[12] (Reboud, Denis, and Ormston 2012).

On ExoMars TGO, the proximity link communications are handled by the *Electra* transponder. Among the improved capabilities of this new generation radio system, the modulation of data volume as a function of the local elevation of the orbiter (i.e. slower when the spacecraft is closer to the horizon, faster when it approaches the maximum elevation) -Webster, Brown, and Cantillo 2016.

Concerning the frequency instability, there is no publication describing this issue for these two specific instruments. MEX is equipped with an oven controlled oscillator (OCXO), which usually has a quite good stability (normally characterised as *Allan deviation*). TGO's radio Electra has a temperature compensated oscillator (TCXO), which are typically at least a factor 10 worse than oven controlled oscillators. Therefore, despite Electra being much more modern, the performance of the internal oscillator is less good than the older MEX one. The Electra on MRO and MAVEN both have OCXO's, therefore they perform much better than the one on TGO (Svedhem 2022).

2.5. SPICE tool

Open-source archives exist for MEX and TGO orbital ephemeris, therefore, when possible, those data will be used. For planetary missions, the most practical source for satellite ephemeris has been identified in the SPICE tool. SPICE is a vast system of tools and datasets developed by NASA (NAIF 2021) that includes and provides 5 different types of information (which together compose the acronym "SPICE"):

1. **S**pacecraft ephemeris
2. **P**lanet ephemeris (including satellites, comets and asteroids)
3. **I**nstrument information (such as field-of-view, size, shape and orientation parameters)
4. **C**-matrix, i.e. information on the spacecraft attitude (or on a spacecraft component upon which science instruments are located)
5. **E**vents information, including summaries of space activities

[12] The Proximity-1 protocol has been designed by CCSDS (Consultative Committee for Space Data Systems) specifically for two-way communication links between a lander and an orbiter. The frequency band used by this protocol is within the 70-centimeter band (CCSDS 2006)

According to the NAIF (Navigation and Ancillary Information Facility) website:

"The primary SPICE data sets are often called kernels or kernel files. SPICE kernels are composed of navigation and other ancillary information providing precision observation geometry for use by the planetary science and engineering communities. SPICE kernels are produced by the most knowledgeable sources of such information, usually located at a mission operations center. SPICE kernels should include or be accompanied by metadata—consistent with flight project data system and SPICE standards—that provide pedigree and other descriptive information needed by prospective users"

SPICE can be used with Python (via the open-source package *SpiceyPy*) providing the *kernel files* described above. Each space mission has its SPICE Kernel dataset; for our simulation, the files that need to be imported from both missions into the Python script are:

1. **fk** Contains definition of reference frames
2. **lsk** Contains a simple text file with the list of leap seconds
3. **pck** Contains generic and mission-specific planetary constants
4. **sclk** Contains the parameters of the spacecraft on-board clock (for synchronization with the ephemeris time)
5. **spk** Different datasets exist for this type of file, including mission analysis, nominal and operational spacecraft trajectory, generic planetary and satellite ephemeris

For our thesis, the online archive for MEX and TGO mission kernels can be found here[13] and here[14] respectively. Depending on the event of interest, the loaded files might change, as trajectory files only cover a limited amount of time (the order of magnitude is days or weeks).
Once the files are correctly imported in our Python environment, a specific function returns the values of position and velocity:

```
[cartesianPosVel] = spiceypy.spkezr(targ, et, ref, abcorr, obs)
```

The documentation for this particular function can be found here[15]. The output is an array of dimension 6 containing position and velocity in Cartesian coordinates, expressed in km and km/s. The input arguments are defined as follows:

- *targ* is simply the target body name, in our case "MEX" or "TGO".
- *et* is the ephemeris time, expressed as seconds past J2000 TDB (Temps Dynamique Barycentrique, or Barycentric Dynamical Time), at which the state of the target body relative to the observer is computed. The ephemeris time refers to time at the observer's location.
- *ref* is the name of the reference frame relative to which the output state vector is expressed. It may be a built-in frame or a frame defined by a frame kernel (FK).
- *abcorr* indicates the aberration corrections to be applied to the state of the target body to account for one-way light time and stellar aberration

The ephemeris time scale (TDB) might seem unpractical (especially as the data for radio-occultation events are expressed in UTC YYYY-MM-DD hh:mm:ss format), but that can be fixed with another built-in function of the *SpiceyPy* package:

```
[et] = spiceypy.str2et(epoch)
```

where *epoch* is a string in the YYYY-MM-DD hh:mm:ss format: therefore we can convert UTC time into TDB time. It is also worth mentioning that, despite TDB and UTC slowly drift apart (Seidelmann and Fukushima 1992), the difference is such that a conversion not including the drift rate would still correctly identify the occultation event within an accuracy of seconds for epochs around 2020. Since we are interested in the event itself (which lasts for minutes) and not in its precise identification in time, we can tolerate any eventual error that may arise from time scale conversions between UTC and TDB. For simplicity reasons (as it is a default coordinate system contained in most *fk* kernels) we will use J2000.0 as a reference frame. This choice surely would make the calculation of the location of occultation events over Mars' surface quite difficult; however, since spherical symmetry conditions apply,

[13] http://spiftp.esac.esa.int/data/SPICE/MARS-EXPRESS/kernels/
[14] http://spiftp.esac.esa.int/data/SPICE/ExoMars2016/kernels/
[15] https://naif.jpl.nasa.gov/pub/naif/toolkit_docs/C/cspice/spkezr_c.html

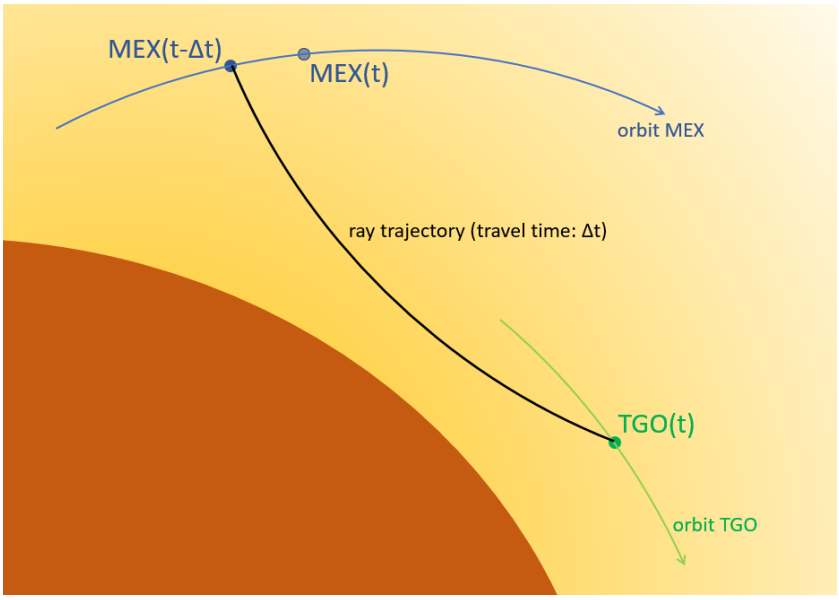

Figure 2.6: Light-time correction; as the photons take time to travel the trajectory path between MEX and TGO, the ones reaching the receiver (TGO) at time t left the transmitter at time $t - \Delta t$, where Δt is the trajectory travel time

information about location is not particularly relevant (once again, we are only interested in the geometry of the trajectory and in the velocity of the spacecraft).
Light-time correction is performed with a dedicated function. This correction is necessary to account for the light travel time: when the photons reach the receiver at time t, they didn't leave the transmitter at time t (which is the state that is returned by SPICE when asked the position and velocity of MEX and TGO at epoch t): instead, what should be considered is the state of the transmitter at epoch $t - \Delta t$, where Δt is the trajectory travel time. To calculate this, we assume that light propagates in a straight line, and we do a first-order correction -the process should be iterative, but a first-order correction is usually enough. To give an idea of the order of magnitude: with a first-order approximation, the position for a transmitter orbiting at an altitude of 400 km and distant 4000 km from the receiver is adjusted by approximately 44 m; an extra iteration would further correct the position by half a millimeter -which is unnecessary accurate for our simulation.

3

Software validation

3.1. Validation of ray-tracing algorithm

The implementation of the Sharma method described in section 2.1 will be validated in two different steps. First, the algorithm will be tested with a known analytical solution for a ray crossing an optically inhomogeneous medium, for which an analytical solution of the ray trajectory is known; second, the Newton-Raphson "homing-in" algorithm will be tested for the same medium, with the purpose of evaluating the rate of convergence. In both cases we use 2D geometry (the algorithms are exactly the same in three dimensions with the addition of the z component).
The selected benchmark is given by a medium whose index of refraction varies along the y component according to this law:

$$n^2(y) = \begin{cases} n_0^2 \left(1 - 2\Delta \frac{y^2}{a^2}\right) & 0 < y \leq a \\ n_0^2 \left(1 - 2\Delta\right) & y > a \end{cases} \tag{3.1}$$

It can be proved (Gómez-Correa et al. 2021) that the trajectory followed by a ray entering the medium at point O(0,0) with an angle θ_0 is:

$$y(x) = \frac{a \sin\theta_0}{\sqrt{2\Delta}} \sin\left(\frac{\sqrt{2\Delta}}{a \cos\theta_0} x\right) \tag{3.2}$$

In fig. 3.1 both the analytical solution and the propagated ray are displayed; the fixed[1] step length for the numerical integration is 0.1 and the ray path is within the interval $x \in [0, 100]$.
Visually, the approximation appears to be acceptable (the two lines are almost indistinguishable). We can plot the difference between the true and the integrated value for different length steps (including $\Delta s = 0.1$ that was used in fig. 3.1) and we obtain fig. 3.2.
The Sharma method, based on Runge-Kutta integration, proved to be extremely accurate: for the benchmark case, a discrepancy in the order of 10^{-13} was found for a length step of 0.01. The improvement in accuracy is coherent to the fact that this is a fourth-order Runge-Kutta method, meaning that the local truncation error is on the order of $O(\Delta s^5)$, while the total accumulated error is on the order of $O(\Delta s^4)$; the error goes from $\sim 10^{-5}$ to $\sim 10^{-9}$ and to $\sim 10^{-3}$ as the length step decreases from $\Delta s = 1$ to $\Delta s = 0.1$ and to $\Delta s = 0.01$ (at $\Delta s = 0.001$ rounding errors become noticeable and the accuracy stops improving). For the simulation of the ray travelling through the atmosphere a similar analysis will be performed to determine the optimal step length for the propagation (see section 3.3).

To test the Newton-Raphson algorithm, we select a target located in proximity of the ascending part of the curve, where trajectory has a monotonic increase of the y component. This is done because for this particular medium, selecting a large value for x could lead to multiple solutions, which is not the

[1] As mentioned in section 2.1, the algorithm used to trace the ray path through the atmosphere adopts a fixed length step; although more computationally demanding, this approach was considered preferable, as it allows to keep integration error sources under control

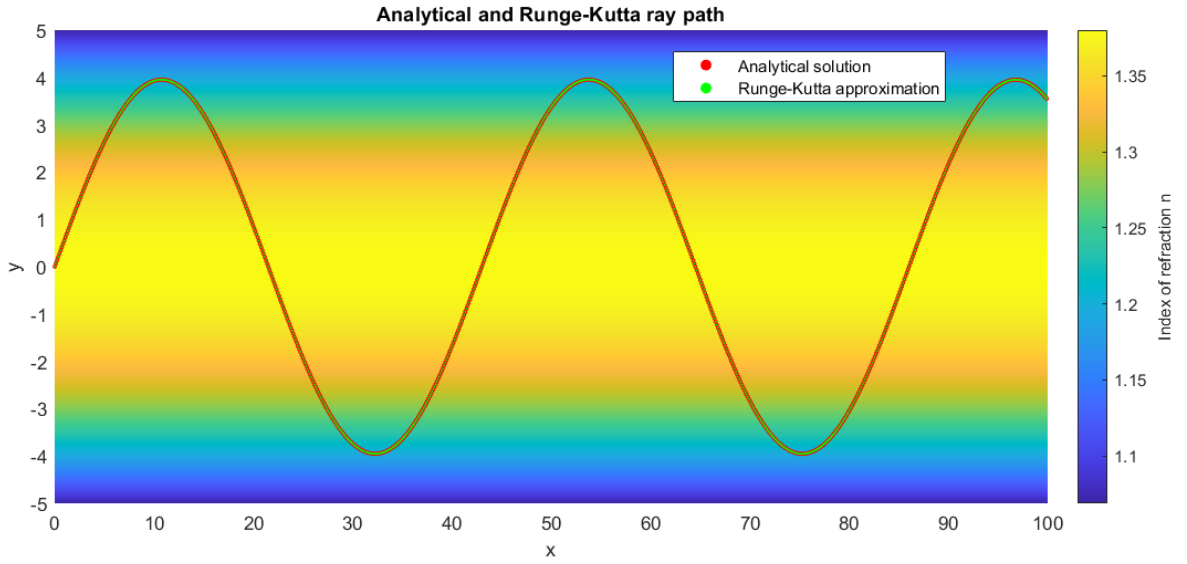

Figure 3.1: Ray path for the n distribution in eq. (3.1). The initial parameters are $a = 5$, $\Delta = 0.2$, $\theta_0 = \pi/6$ and the (fixed) length step is 0.1

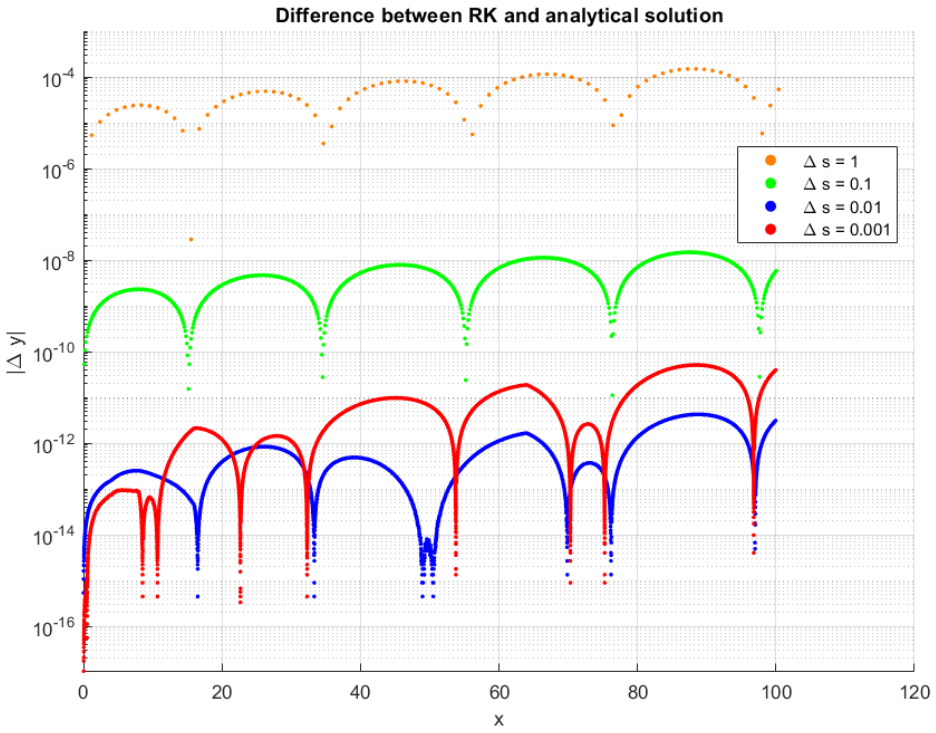

Figure 3.2: Absolute value of the difference between real value and value obtained through Runge-Kutta ray integration. The initial parameters are the same used in fig. 3.1 Ray path for the n distribution in fig. 3.1. The length steps that have been tested are $\Delta s = 1$, $\Delta s = 0.1$, $\Delta s = 0.01$, $\Delta s = 0.001$

expected outcome from our atmospheric model: therefore we restrict our x domain to a region where the ray solution is one and one only.
The algorithm is tested for different points in the aforementioned region. Given a length step of 0.001 and a stop condition of 10^{-6} (i.e. convergence is reached when the ray path misses the target by a distance smaller than 10^{-6}) convergence is usually reached in ~ 5 iterations. This is a preliminary test for the Newton-Raphson algorithm that has been designed: it only proves its capability to converge to the correct solution for a particular case. The real test is on the atmospheric simulation itself.

3.2. Validation of simulated frequency residuals with real-world data (MEX-TGO mutual occultation)

Data from an occultation event between MEX and TGO are shown in fig. 3.3. The occultation event happened on April 6th 2021, starting at 03:40:00 UTC; during the ingress occultation the distance between the two spacecraft varied between 4395 and 5890 km; the local solar time was 11h, with a solar elevation angle of 55° (day time occultation); the altitude range for the ray trajectory varied between 387 and 0 km. Four main features can be observed:

1. The free-space residual frequency measurement has a noticeable level of noise (approximately, between 0 and 350s of elapsed time)
2. There is a clear signal from the ionosphere (peak at 444s)
3. There is a secondary peak at 468s, probably due to a secondary ionospheric layer at lower altitudes; the existence of this layer is well known (and has been explicitly described in section 2.2), but it has not been included in our model
4. A downward trend observable from 516s of elapsed time is the mark of Mars' troposphere

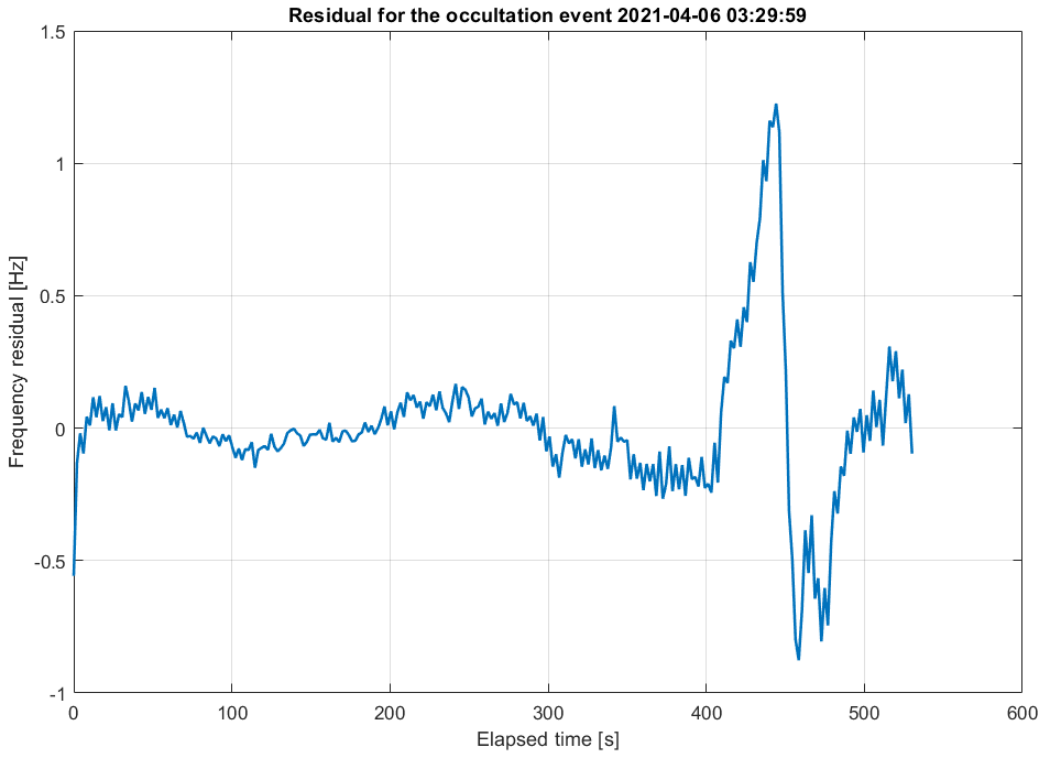

Figure 3.3: Residual for the occultation event 2021-04-06 03:29:59

A comparison between our model and occultation data can be seen in fig. 3.4. Despite the similar shape, it is immediately noticeable that our model exceeds the measurements maximum and minimum values. This can be explained by considering what makes our model a "worst-case scenario":

1. The ionospheric profile of the model describes electron density at the *sub-solar point*: our measurements are taken with a local solar elevation angle of 55°
2. The model assumes a perihelion Sun-Mars distance; the occultation event took place 3 months before aphelion[2]
3. The measurements occurred at the beginning of solar cycle 25, with a relatively low solar activity[3]; the model assumes maximum solar activity

It is therefore not surprising that the model diverges from measurements; moreover, as we ignored the secondary ionospheric layer, the signal plummets at around 461s of elapsed time, while in reality the existence of this additional ionized region of the atmosphere keeps the frequency residual signal above -1Hz.
From these real measurements we can retrieve a crucial information for our thesis, the expected measurement noise; considering the time span between 0 and 350s ("free space" communication link), the σ for the measurement noise is ≈ 0.09 Hz: this is the number to be used as a reference when analyzing the performance of the straight line approximation.
One last element worth mentioning is the sampling rate of TGO's receiver. Frequency measurements are available at time intervals of ≈ 2.0470 s, whereas our simulation returns frequency shift values every second. This does not have any practical consequence on our simulation, but it can be relevant for the optimization technique described in section 1.2: in this type of problem one needs the number of parameters n to be significantly smaller than the number of measurements m ($n << m$). If we consider this event to be representative for the average duration of a Martian radio occultation measurement, and assuming that relevant a clear atmospheric footprint appears at epoch $t \approx 350$ s, we are left with a series of 88 distinct measurements; therefore, given the previous assumptions, $n << 88$.

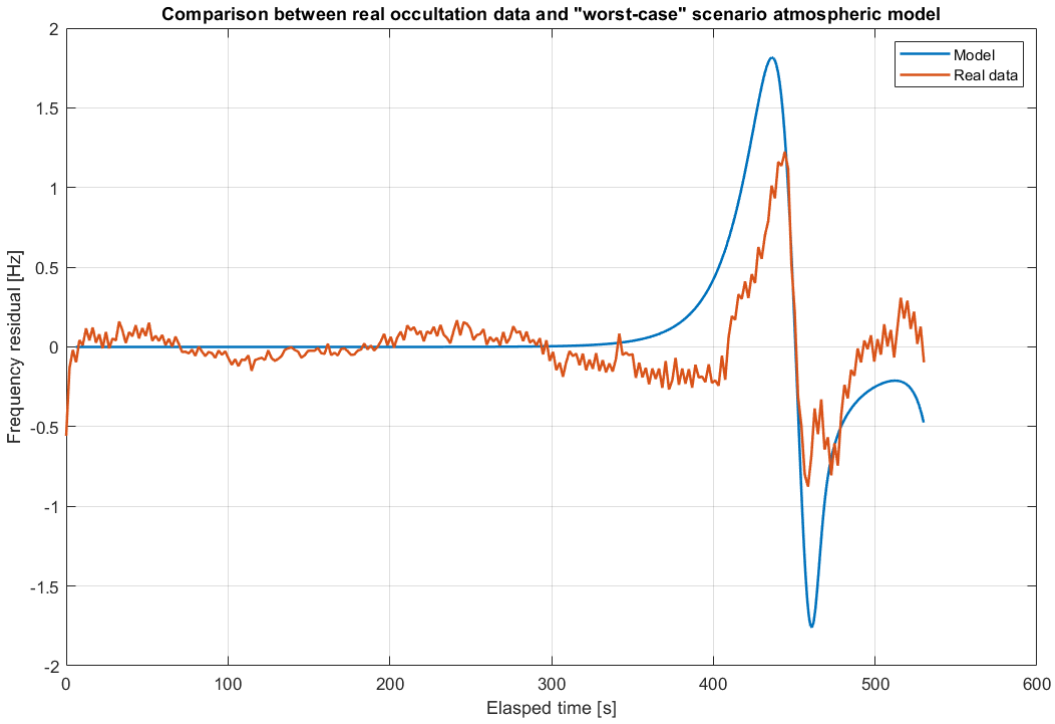

Figure 3.4: Comparison between real occultation data and "worst-case" scenario atmospheric model for Martian ionosphere

3.3. Parameter calibration

Two key parameters must be calibrated for the ray path simulation through Martian atmosphere: the spatial step length Δs and the temporal step length Δt. For the calibration we will use orbital data

[2]Source: https://www.heavens-above.com/PlanetSummary.aspx?lat=0&lng=0&loc=Unspecified&alt=0&tz=UCT
[3]Source: https://www.swpc.noaa.gov/products/solar-cycle-progression

from the occultation event of December 1st 2020, 18:04:00 TT. This particular occultation, as the one described in section 3.2, is an *ingress* event therefore the ray, after travelling through vacuum, first crosses the ionosphere and then, in the very last seconds, the lower neutral layers of Mars' atmosphere. For the *spatial step length* Δs, we run the simulation of the occultation event and calculate the value of the total phase Φ for both the curved path and the straight line approximation. The value of Φ is calculated via simple Euler integration:

$$\Phi = \frac{2\pi}{\lambda} \sum_{i=1}^{N} n_i \Delta s_i \tag{3.3}$$

where n_i is the index of refraction at the midpoint between point i and $i+1$ for $i = 0, 1, ..., N$. The results are shown in fig. 3.5 (curved line) and fig. 3.6 (straight line). The benchmark for the error estimate is the total phase output given by selecting $\Delta s = 10$ m as step length[4] -which, for the machine time required, would be unpractical for common use). As it can be seen from the plots, rounding errors occur at higher values of Δs for the simpler straight method. The recommendation would therefore be to use $\Delta s = 300$ m for the curved line and $\Delta s = 1000$ m for the straight line.

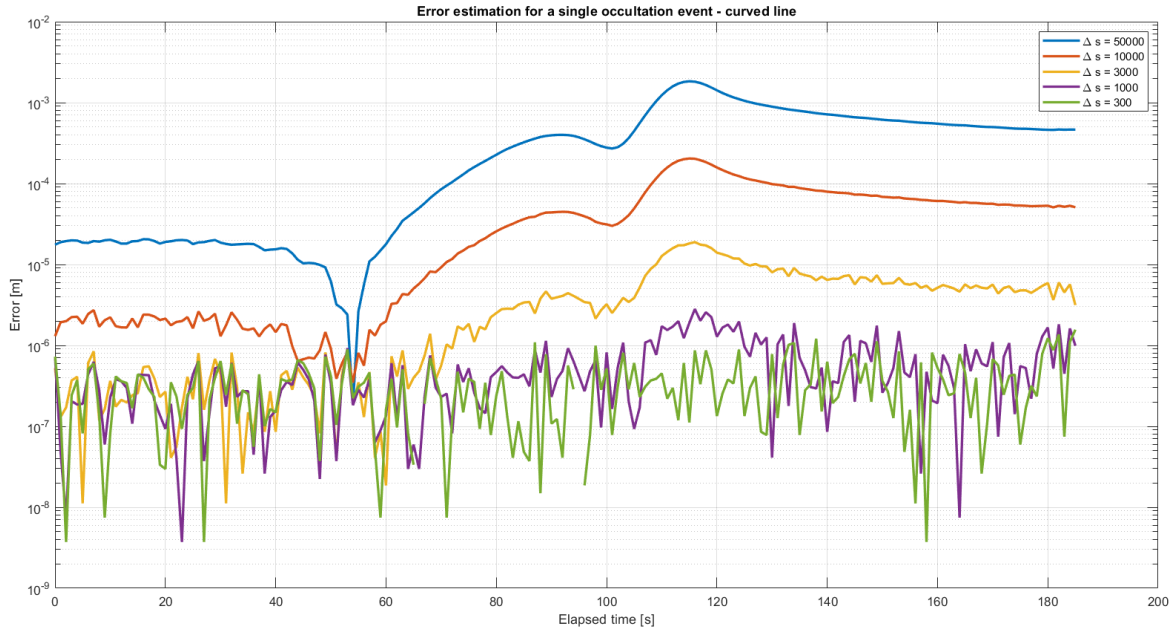

Figure 3.5: Absolute value of error for different spatial step length in the estimation of the total phase Φ for the curved line ray trajectory

For the numerical differentiation, we will make use of the *symmetric difference quotient* (or *three-point centered-difference formula*) for the calculation of the frequency shift (which is proportional to the time derivative of the total phase). The formula for this numerical derivation is:

$$f'(x) \sim \frac{f(x+h) - f(x-h)}{2h} \tag{3.4}$$

with an estimated error of $-(1/6)f^{(3)}(c) \cdot h^2$ (where $c \in (x-h, x+h)$). In floating-point arithmetic, h cannot be as small as we want: below a certain value, the achievable accuracy rapidly deteriorates due to *loss of significance*[5] (Sauer 2011). Therefore, we need to find values for h that minimize truncation error but do not trigger loss of significance effect. In double precision, the value is approximately:

$$h_{optimal} \sim \sqrt[3]{\epsilon_{machine}} \approx 10^{-5} \tag{3.5}$$

[4] This number has been selected as it proved to be low enough to let rounding errors emerge from the error analysis which is what one wants to see to select the optimal step length

[5] This behavior emerges as, for small values of h, the subtraction occurs between nearly equal numbers -therefore losing significant digits- and then the result is divided by a small number

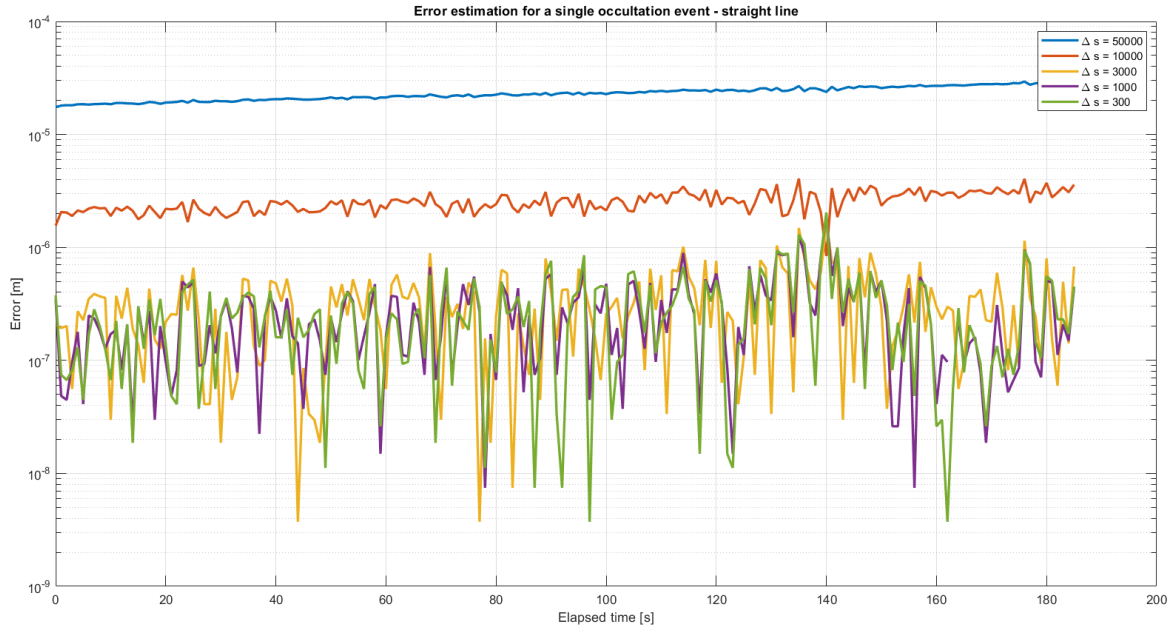

Figure 3.6: Absolute value of error for different spatial step length in the estimation of the total phase Φ for the straight line approximation

The current version of the algorithm does not have the required numerical stability to unambiguously identify an optimal value for h. However, by comparing the output from the curved line and the formula approach (which should yield the same result), it appears that by adopting $h = 2^{-13}$ or $h = 2^{-14}$ the error in the frequency shift estimation remains in the order $10^{-4} - 10^{-5}$ Hz, which proves to be enough for the signal we need to analyze (see section 3.2).

4

Results

4.1. Simulated Doppler profiles for Mars' atmosphere

After calibration, the simulation can be executed for the selected occultation event. The output is the one shown in fig. 4.1, where the plots represent (from top to bottom):

1. The Doppler effect from satellite motion *only* (i.e. only considering relative velocities)
2. The phase shift rate calculated for the *path of minimum time* (what we called the "curved line", using the formula from Fermat's theorem and calculus of variation) and the phase shift rate calculate with numerical differentiation for the straight line approximation
3. Difference between values calculated at point 2. and the Doppler effect at point 1: it is the so-called "frequency residual", which corresponds to the atmospheric effect (the same type of plot shown in fig. 3.4)
4. Difference between the two signals at point 3 (therefore, the difference between curved-line and straight-line frequency shift).

The results are consistent with the simulations executed by the ROMA project (Nava et al. 2020), which returned similar profiles with a comparable order of magnitude. Another confirmation comes from the analysis of the *bending angle* α, which is almost exactly twice as large as in the ROMA project simulation: this is due to the fact that the selected ionosphere (which is the main responsible for the bending angle) is twice as dense as the one in Nava et al. 2020[1] (see fig. 4.2).
For the Martian atmosphere simulation, the "homing-in" algorithm always converged to a solution, 100% of the times requiring less then 5 iterations; given the "smoothness" of the plot is it reasonable to believe that no "alternative paths" exist in the proximity of the identified raypath (no observable multipath originating from the mathematical expression of the ionospheric and tropospheric index of refraction).
The frequency shift residuals obtained with the two approaches do not differ more than 0.07 Hz (minimum value in the the last plot of fig. 4.1). This difference appears to be small, especially if compared with the signal noise calculated in section 3.2 (which was approximately 0.09 Hz). However, this information alone is not enough to state whether the straight line hypothesis is in fact a good approximation: one must verify what is the impact of such a difference on the calculation of the atmospheric parameters; in particular, what is the impact in the estimate of the index of refraction n profile.

4.2. Sensitivity analysis for the straight line approximation

The last plot in fig. 4.1 displays the error introduced by the straight line approximation when calculating the residual frequency shift. We see that the difference is in the order of tens of millihertz, which appears to be negligible when compared to the magnitude of the signal (see third plot from the top in fig. 4.1) and to the signal noise calculated in section 3.2.

[1] For comparison, he model used in Nava et al. 2020 assumes a simple Chapman distribution where $h_{m,0} = 130$ km, $H = 15$ km and $N_{e,0} = 10^{11}$ e^-/m^3, whereas our model uses $h_{m,0} = 132,4$, $H = 13.3$ km and $N_{e,0} = 2 \cdot 10^{11}$ e^-/m^3; clearly the most noticeable difference is the parameter for the electron density

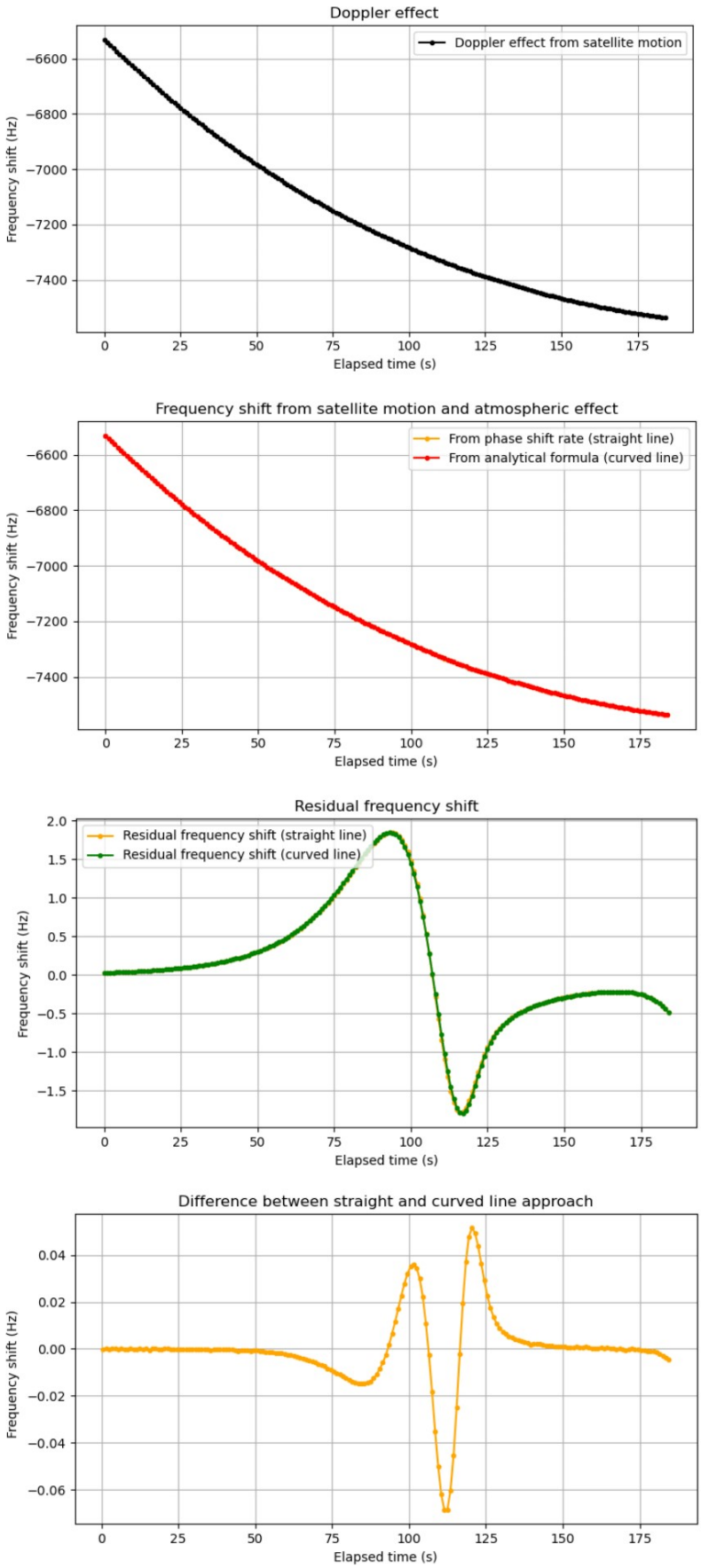

Figure 4.1: Simulation of the occultation event ”14-12-2020 18:04:00”

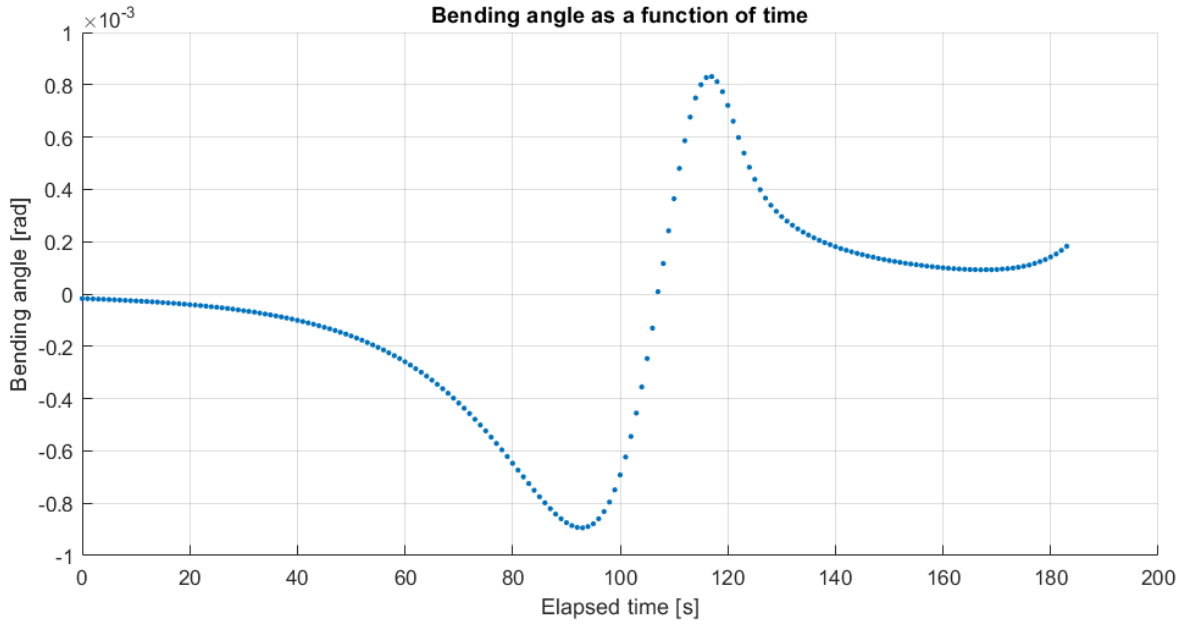

Figure 4.2: Simulation of the bending angle resulting from the occultation event ”14-12-2020 18:04:00”

The effect that this difference has on the estimation of atmospheric parameters will be assessed via the *Abel transform*. This mathematical tool (see section 1.2) allows to calculate the index of refraction at a certain height given the distribution of ray's bending angle and impact parameters *above* that height. The formula is:

$$n(r) = \exp\left(\frac{1}{\pi}\int_{a_1}^{\infty} \frac{\alpha(a)}{a^2 - a_1^2} da\right) \tag{4.1}$$

where α is the bending angle and a is the impact parameter (see fig. 1.3).
Abel transform only works within the spherical symmetry hypothesis (which allows the definition of a unique bending angle and impact parameter for any given ray crossing the atmosphere). It is by definition the inverse of the algorithm performed to calculate the frequency shift: therefore, if we insert the values of $\alpha(a)$ obtained from the ”curved” trajectory (i.e. the values corresponding to the ”real” ray path) into eq. (4.1), the output should be the nominal profile $n(r)$ used in the simulation.
Knowing this, the error introduced by the straight line approximation will be estimated as follows. We assume that the frequency shift signal resulting from the straight line approximation is in fact the result of a ”real” propagation (i.e. a propagation that follows Snell's law); with the values of the frequency shift we can calculate ”virtual” bending angles and impact parameters, from which the $n(r)$ profile can be calculated using eq. (4.1); the difference between this $n(r)$ profile and the nominal one is a reliable estimate of the error introduced by the straight line approximation.
This method requires to calculate $\alpha(a)$ and a from the frequency shift measurements. Equation (2.18) provides an expression for the frequency shift, which can be turned into an explicit equation with the impact parameter a being the only unknown quantity:

$$\lambda f_D = \left(\sqrt{r_R^2 - a^2} - \sqrt{r_R^2 - b^2}\right)\frac{\dot{r_R}}{r_R} + \left(\sqrt{r_T^2 - a^2} - \sqrt{r_T^2 - b^2}\right)\frac{\dot{r_T}}{r_T} + (a-b)\left(\dot{\theta}_T - \dot{\theta}_R\right) \tag{4.2}$$

where the meaning of each term can be found in fig. 4.3. Compared to eq. (2.18), this equation assumes that $n_A = n_B = 1$, which is a reasonable hypothesis for both satellites[2].
Once the impact parameter at epoch t is calculated, the corresponding bending angle α can then be

[2]It is also a *forced* hypothesis, since we are assuming there is no *a priori* knowledge of the refractivity profile: for satellites orbiting at ionospheric altitudes, this is a well-known source of error (see Kursinski et al. 1997)

found as the solution of eq. (4.3):

$$\begin{cases} a = r_R \sin(\delta_R + \chi_R) \\ a = r_T \sin(\delta_T + \chi_T) \\ \alpha = \delta_R + \delta_T \end{cases} \tag{4.3}$$

Once $\alpha(a)$ is known, we can numerically calculate the integral contained in the Abel transform. It is worth mentioning that the integral in eq. (4.1) converges, but that in practice it is impossible to obtain high values of a: for mutual satellite occultations, the value is usually limited by the altitude of one of the two satellites. In our case, the limiting factor is the altitude of TGO: therefore, a cannot be larger than $\approx R_{Mars} + 400$ km. This is a well-known issue in radio occultation techniques, called the *upper boundary problem* (a complete description of this problem can be found in Kursinski et al. 1997). Since we can select the initial epoch of our simulation, we can set it in such a way that the line-of-sight between the two spacecraft is high above the surface of Mars: this first observation will be the upper limit of the integral in eq. (4.1). We selected a starting configuration for which the maximum height above the surface of the line of sight is ≈ 340 km where, according to our ionospheric model, electron density is lower than the peak density by a factor smaller than 10^{-3}.

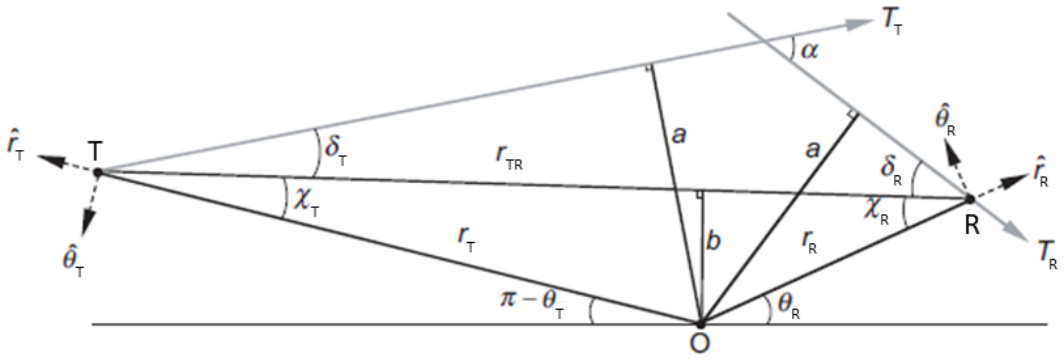

Figure 4.3: In-plane geometry of a radio occultation event (adapted from Melbourne 2004)

The results of the Abel transform are shown in fig. 4.4. The dashed green line represent the nominal index of refraction profile. The other two lines are the output of Abel transform: the **magenta** and **blue** lines are obtained via inversion of frequency shifts in the "curved-line" propagation and straight-line approximation respectively.
In principle, the magenta line should match the dashed green line *exactly*: any observed discrepancy is due to all the integration approximation performed (in the ray trajectory estimation and in the Abel transform calculation); these sources of error are the same that affect the straight line approximation, therefore we will use the magenta plot as the true benchmark to assess the goodness of the straight line approximation.
The differences in the three plots are hardly noticeable. The index of refraction can be converted into electron density with eq. (2.20). By applying this formula we can determine that the difference between the dashed green line and the magenta line (i.e. the error introduced by numerical integration) nominal $n(r)$ corresponds to an error in the estimate of the electron density peak of 0.04%. For the neutral species in the lower atmosphere, the error introduced by numerical integration corresponds to a 0.57% error in the estimate of low altitudes (specifically, at $h = 2000$ m and assuming an isotermic atmosphere).
The same comparison can be done between the magenta and the blue line (as we stated above, the magenta line is the true benchmark for the straight line approximation). When comparing the two output, the difference in the estimate of ionospheric electron density peak is 0.25%, while the difference in the retrieved tropospheric, low-altitude pressure is about 0.50%. It is therefore clear that, from a mathematical point of view, the error introduced by assuming a straight line propagation in a spherically symmetric atmosphere at Mars is relatively small.

It is worth comparing these results with a similar simulation using Earth parameters, as in terrestrial

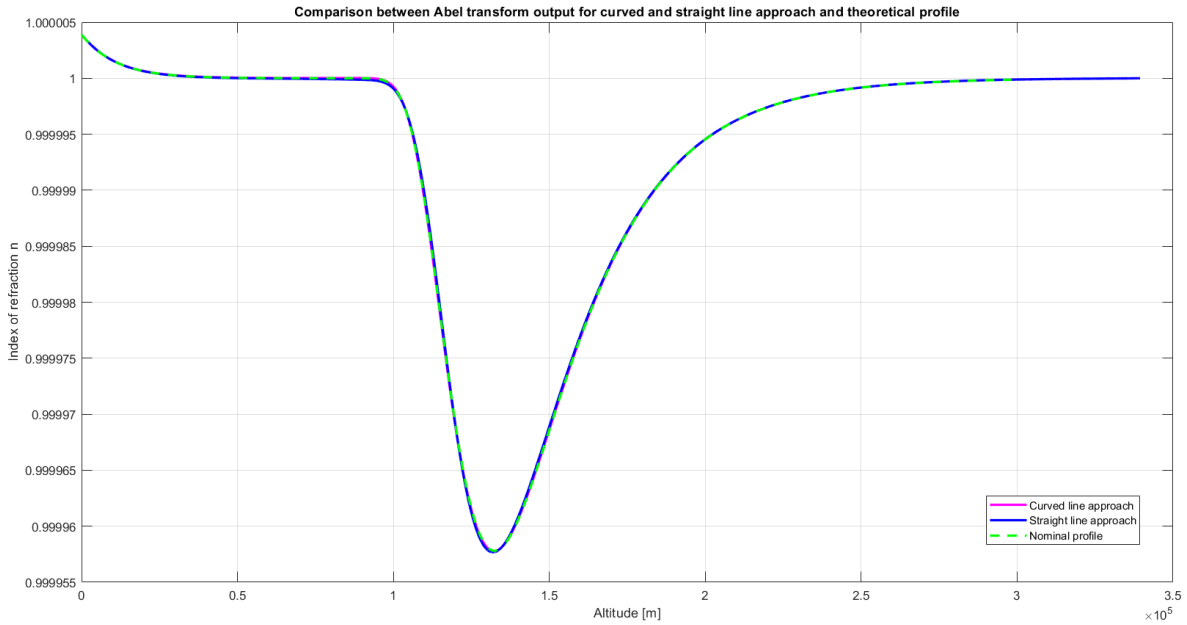

Figure 4.4: Output from Abel transform, compared with the nominal profile for the index of refraction (in **green**)

orbit inter-satellite link for radio occultation measurements have been (and currently are) widely used (see chapter 1). As this simulation only provides a term of comparison for the Martian results, we can model the orbits of the two spacecraft around Earth in a convenient way, therefore adopting a simplified geometry with a monotonic Doppler effect and high values for the impact parameters (to obtain a more precise signal after Abel transform). The simulated trajectories are the ones of two satellites flying in co-planar, circular orbits at 2000 km of altitude (high enough to avoid the *upper boundary problem*), moving in opposite directions and separated by an initial angle $\eta = \pi/9$. The frequency used to model the ionospheric effect is the same as the inter-satellite communication link between MEX and TGO (437.1 MHz)[3]. The results of this simulation are shown in fig. 4.5.
The first thing that should noticed is that the magnitude of the atmospheric effect (third box from the top in fig. 4.5) is larger than on Mars, both for the ionosphere (from epoch t=350s to t=620s) and the neutral atmosphere (mostly visible after t=620s). This was expected, as both electron density and neutral gas density is much higher on Earth than on Mars. Moreover, it is immediately visible that the straight line approximation (yellow line inside the third plot from top in fig. 4.5) visibly diverges from the ”real” frequency shift for lower ray heights[4], where the signal crosses the densest part of Earth’s troposphere. There, the bending effect simply cannot be neglected and the straight line approximation clearly fails.
As it has been done in the Martian case, we invert the frequency shift measurements with the Abel transform for both the curved line trajectory and the straight line approximation to obtain the refractivity profile: the results of this inversion are displayed in fig. 4.6. As expected from the large difference found in fig. 4.5, the straight line approaches fails in returning acceptable values of refractivity for lower altitudes. However, it returns a very close approximation for the ionospheric peak. The numerical integration error (difference between the nominal profile and the one obtained by Abel-transforming the frequency output from the curved line propagation) in the estimate of the peak electron density is 0.034%, while the error introduced by the straight line approach (difference between blue and magenta line, i.e. deviation of the straight line from the curved line) is 0.28%

[3] Despite we use this value of frequency to make a homogeneous comparison, this does not correspond to a radio signal that would commonly be used for this purpose. On Earth, inter-satellite ionospheric measurements are performed with GPS signals. All GPS satellites transmit *at least* two circularly polarized signals at two frequencies, designated as L1 and L2; the GPS carrier signal L1 has a frequency of 1575.42 MHz, while signal L2 is centered at centered at 1227.60 MHz. Therefore, the use of a carrier frequency of 437.1 MHz *amplifies* the ionospheric effect, as the refractivity of the ionospheric plasma is proportional to $1/f^2$

[4] The last diagram in fig. 4.5 does not show the last 5 points of the plot, which drops down to to -50 Hz in the last seconds of the occultation event

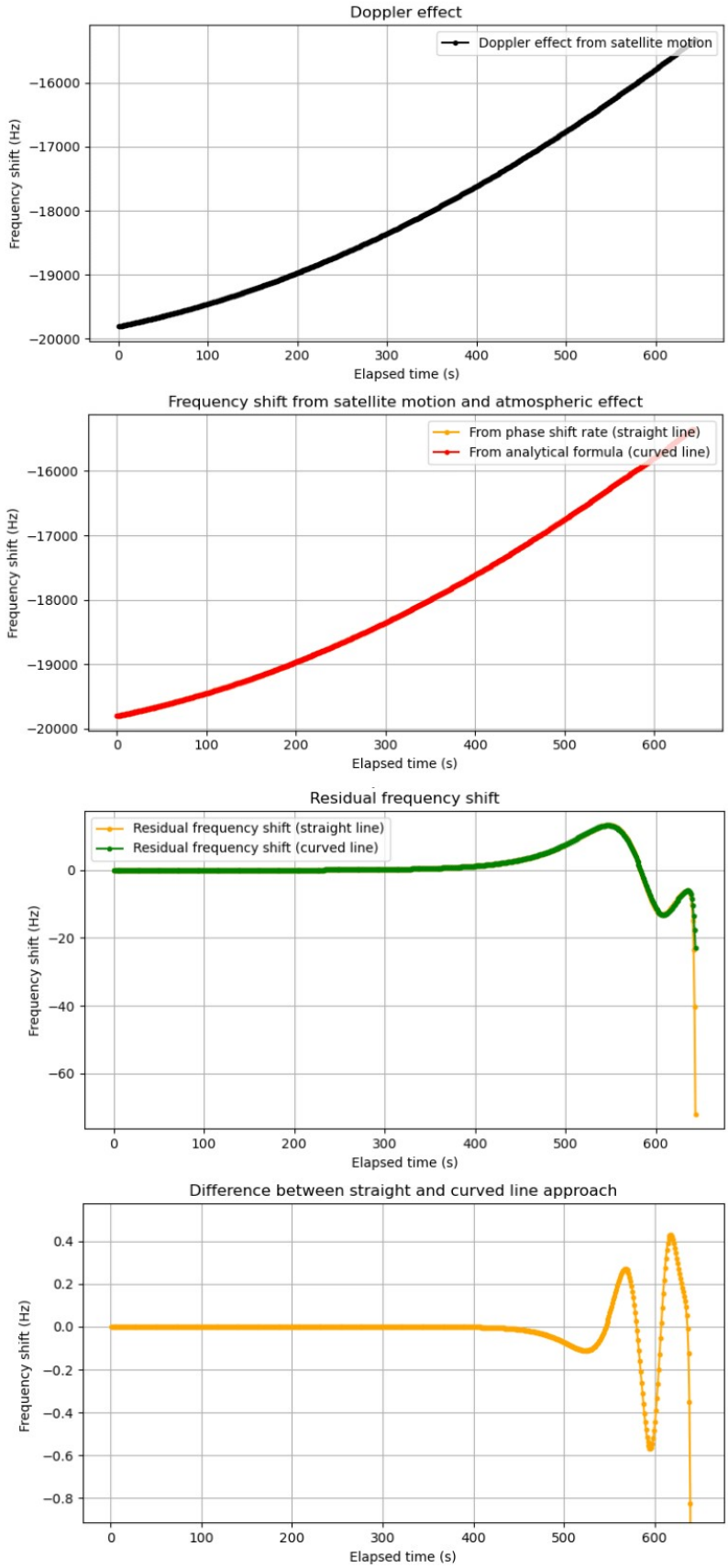

Figure 4.5: Simulated occultation event for Earth atmosphere; the plotted quantities are the same as in fig. 4.1

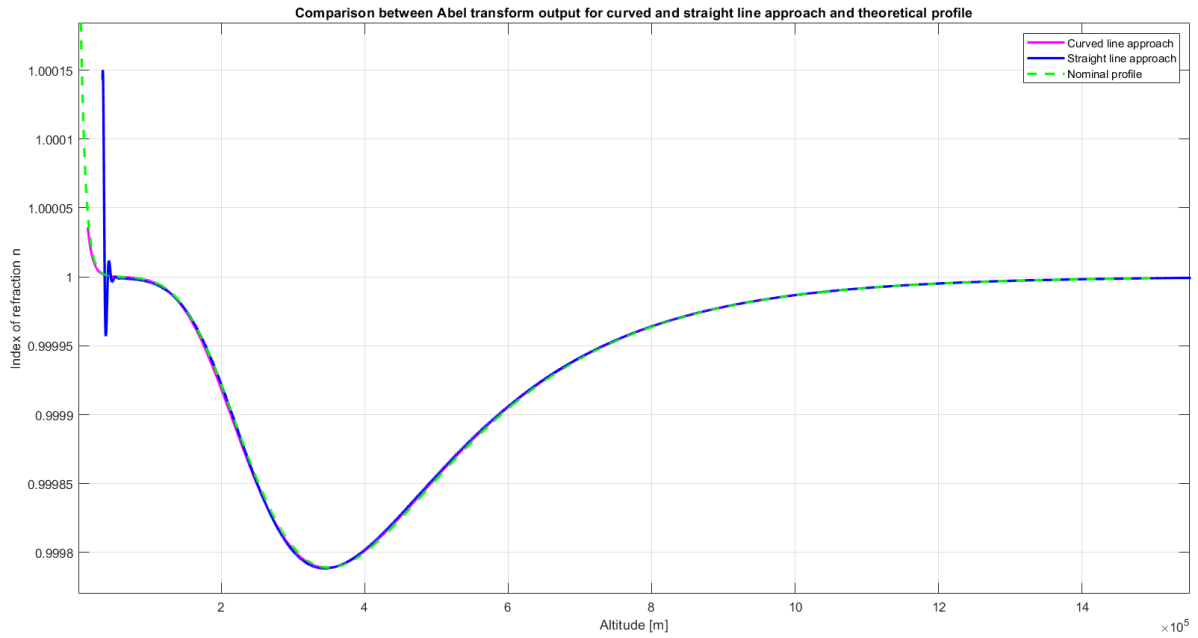

Figure 4.6: Output from Abel transform, compared with the nominal profile for the index of refraction (in **green**) for a simulated occultation event on Earth

4.3. Effect of asymmetric atmosphere on frequency shift estimation

The study performed in the previous section proved that, if one assumes that the ray between transmitter and receiver propagates in a straight line during a Martian mutual occultation event, the error introduced by this approximation in the estimate of the atmospheric effect (i.e. the effect on the *residual frequency shift*, which is the total frequency shift measured by the receiver minus the Doppler effect due to satellite motion) is negligible. In particular, the estimate of *ionospheric effect*, simulated for Mars and Earth, is scarcely affected by the straight line approximation; on the other hand, the estimate *tropospheric effect* can be significantly affected by the straight line approximation for thicker atmospheres (Earth) but on Mars the difference is, once again, negligible.
In this section we will inquire whether the goodness of the approximation stands the test of *horizontal gradient*. When spherical symmetry hypothesis is abandoned, ray theory tells us that (in general) the ray is not confined anymore in a two-dimensional plane: the off-plane trajectory component might consequently affect the adequacy of the straight-line approximation: results found in section 4.2 might no longer be valid, therefore a separate discussion is needed.
As showed in section 4.1, the major contribution to the atmospheric effect comes from the ionosphere. The most significant asymmetry in the ionosphere is the day-night variation in ionospheric electron density -in the upcoming simulation, we will ignore the day-night difference in pressure and temperature for the neutral atmosphere. In practice, we will replicate the simulations of section 4.1 with an asymmetric ionosphere, which will take the form of a classic Chapman profile (see eq. (2.21)), this time including the Chapman grazing function (and therefore the dependency from the solar zenith angle χ).

Two different simulations will be performed: an occultation event taking place on the sunlit side and an identical occultation event (i.e. with the same mutual orbital configuration between the two spacecraft) occurring over the terminator line.
For the first simulation, the Chapman grazing function $Ch(h, \chi)$ will be approximated by $\sec \chi$ alone: this is considered to be a satisfactory approximation for solar zenith angles below $75°$ (see section 2.2). The two "virtual" spacecraft operating the mutual occultation measurements fly in two circular, co-planar orbits with the same altitude, both departing from a starting point on the sunlit hemisphere. The starting point can be selected as a *local maximum in the gradient of the index of refraction*: in this way, the ray will undergo through the maximum possible bending, therefore maximizing the error introduced by the

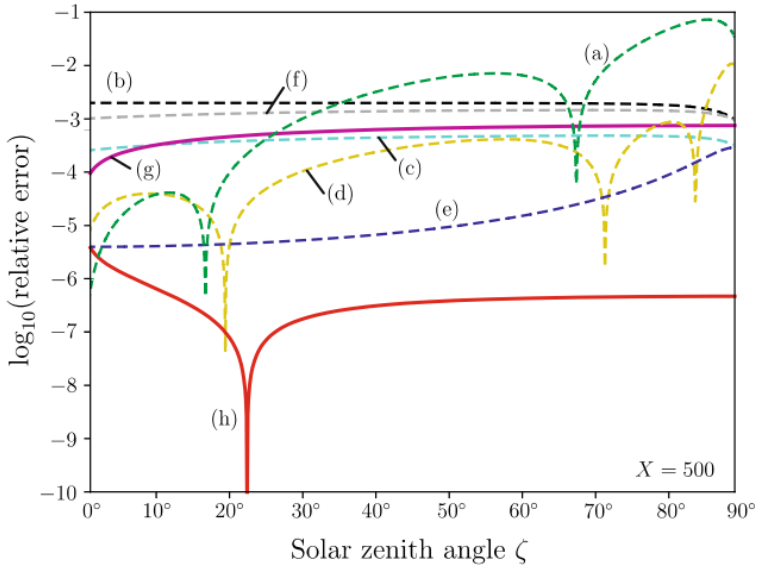

Figure 4.7: Fitzmaurice formula compared with other numerical methods for the approximation of Chapman grazing function (image from Vasylyev 2021)

straight line approximation. If we look for a gradient maximum at peak height $h_{m,0}$, results show that the maximum gradient occurs at $x = R/4$ (where the x-axis points towards the Sun and $R = R_M + h_{m,0}$). For a selected initial altitude of 450 km, this point is located at a solar zenith angle of 75.52°: too close to the terminator to use the secant approximation. As a trade-off, since the gradient grows monotonously, we can select a location close enough to the $x = R/4$ that allows us to simulate radio occultation events at different orbital inclinations. According to this definition, the starting point is located at a solar zenith angle of 47°

For the second simulation, the ”secant approximation” is inadequate. It is so because at the terminator the solar zenith angle is larger than 75°, but the real reason can be deduced from the shape of the Chapman distribution for $Ch(h, \chi) = \sec \chi$: the formula implies that the electron density drops to 0 at the terminator for any given altitude and that it remains constant at 0 over the entire night side of the planet. The fact that at the anti-solar point (i.e. the ”midnight point”) the electron density has a much smaller value than the sunlit side is acceptable, but the abrupt drop to 0 at the terminator line is unrealistic; therefore, a more sophisticated form for the Chapman grazing function is required. The most recent analytical approximation of eq. (2.22) can be found in Vasylyev 2021: it proves precise even for lower values of χ, but the formula is quite complex and computationally heavy. A compromise solution is using the so-called ”Fitzmaurice formula” (Fitzmaurice 1964), which has a simpler analytical expression:

$$Ch(X, \chi) = \sqrt{\frac{\pi X}{2}}\ \mathrm{erfc}\left(\sqrt{\frac{X}{2}}\cos\chi\right)\exp\left(\frac{X}{2}\cos^2\chi\right) \tag{4.4}$$

where X is the ratio between $R_{Mars} + h_{sat}$ and the scale height H, while ”erfc” is the complementary error function defined as:

$$\mathrm{erfc}(z) = 1 - \mathrm{erf}(z) = 1 - \frac{2}{\sqrt{\pi}}\int_0^z e^{-t^2}\,dt \tag{4.5}$$

The Fitzmaurice formula has the advantage of being relatively easy to differentiate, compared to the other formulations described in Fitzmaurice 1964 and shown in fig. 4.7. In particular, fig. 4.7 shows 8 different methods to approximate the Chapman function[5]; it is noticeable that, although the Fitzmaurice formula (marked with (b)) does not particularly well for low values of the solar zenith angle, as one gets closer to the terminator ($SZA = 90°$) many of the methods converge to a relative error of approximately

[5]This diagram shows the relative errors for a value of $X = 500$, where X, the ratio between the orbit radius and the scale height of the ionosphere, is the same quantity that appears in eq. (2.22). In our case, $X \approx 290$, which is a bit far from the value prescribed. However, in the same paper another plot shows similar results for $X = 50$, therefore we can safely assume that the conclusions drawn for Fitzmaurice formula are valid

10^{-3} (the one that outperforms all the others -the red plot- is the innovative method proposed in the paper, which however has quite a complex formulation).
The Chapman grazing function can be extended to $\chi > 90°$ with the following modifications (Fitzmaurice 1964):

$$Ch(X,\chi) = 2\exp(X - X\sin\chi)Ch(X\sin\chi, \pi/2) - Ch(X, \pi - \chi) = \tag{4.6}$$

$$= 2\exp(X - X\sin\chi)\sqrt{\frac{\pi X\sin\chi}{2}} - \sqrt{\frac{\pi X}{2}}\,\mathrm{erfc}\left(-\sqrt{\frac{X}{2}}\cos\chi\right)\exp\left(\frac{X}{2}\cos^2\chi\right) \tag{4.7}$$

Once again, in our simulation the x-axis points towards the Sun, therefore the χ angle is given by the simple equation:

$$\cos\chi = \frac{x}{R} = \frac{x}{\sqrt{x^2 + y^2 + z^2}} \tag{4.8}$$

Once the grazing functions for the sunlit hemisphere and for the terminator occultations are defined, the simulation can be executed using the same ray-tracing and homing-in algorithms described in section 2.1 (with the fundamental difference that this time they include 3 dimensions).
After the first simulation is executed and the results plotted, it is immediately noticeable that the output (fig. 4.8) resembles the one in fig. 4.1 (last plot): the shape is the same and so is the order of magnitude of the difference between the two propagated ray paths, although slightly smaller. This can be explained by noticing that the region sampled during the occultation is relatively small compared to the circumference of the planet, therefore a strong signal from the now-introduced asymmetry would appear if the gradient of n displays strong local variations. However, even though we selected a local maximum in the index of refraction gradient, the trend of Chapman grazing function $Ch(h,\chi) = \sec\chi$ for angles lower then $\approx 75°$ is such that the electron density (and therefore, the index of refraction) still varies relatively slowly with the solar zenith angle.

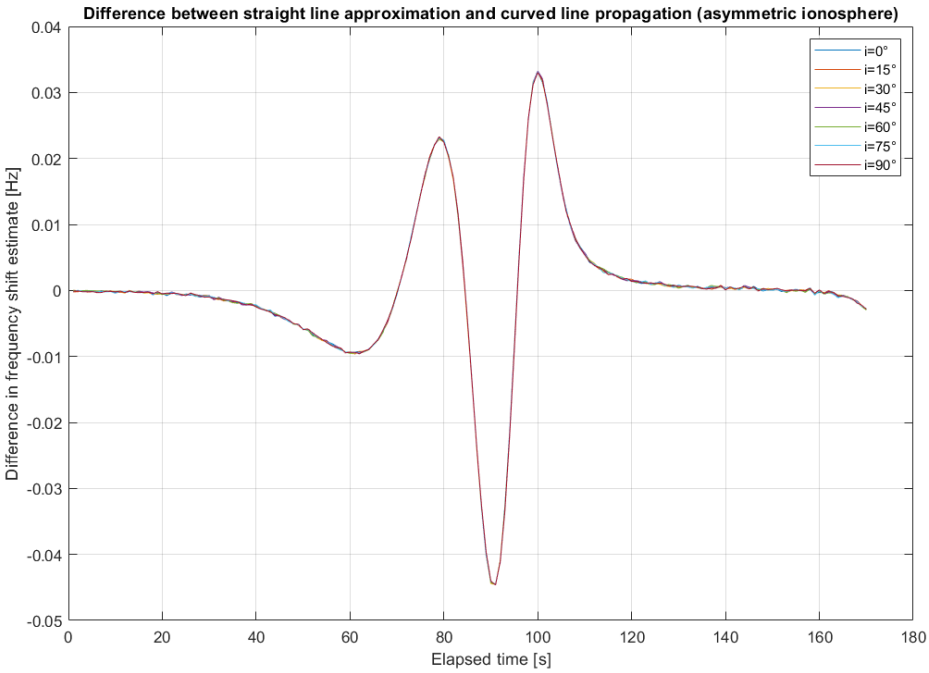

Figure 4.8: Difference between frequency shift calculated with the "straight line approach" and with the formula for real (curved) rays for seven different inclinations

Another interesting feature is that the plot (which represent the error introduced by the straight line approximation) does not show any significant dependency from the orbital inclination; this is most likely another hint of the fact that vertical gradient, in the model created, is by far the driving force of atmospheric frequency shift, at least with the type of asymmetry introduced.
The last detail that can be noticed is the jagged appearance of the plot towards the left and right

extremes of the plot. It would be reasonable to expect a smooth line, and no clear reason for these irregularities emerged. A possible explanation is that the asymmetry introduces a *multipath effect*: the solutions (i.e. the possible ray paths) are not too different between each other and the algorithm does not converge to the "same" trajectory at all epochs. According to this interpretation, this effect exists at any given epoch, and it is just more noticeable at the beginning and at the end of the occultation event only because the horizontal trend of the plot makes it more visible.
For this case and for the next one a sensitivity analysis for the introduced error will not be performed, as the "fast" method used in section 4.2 is no longer applicable. In this case, our observations will stop at the absolute error introduced by the straight-line approximation, which never exceeds 0.05 Hz: by analogy with the spherical symmetric case, we can infer that this error is small, and introduces a minor deviation in the estimation of atmospheric parameters.

For the terminator occultation, we use again two circular, co-planar orbits at $h = 450$ km, flying in opposite direction from an initial point located above the terminator line. As mentioned above, the ionospheric model is here integrated with a more sophisticated Chapman grazing function, that is able to return values of N_e for $\chi > \pi/2$. The effect of this additional function on ionospheric density profile is displayed in fig. 4.9, where the equatorial electron density is plotted at different altitude for both the simplified function $Ch(\chi) = \sec\chi$ and the Fitzmaurice formula. It is clearly noticeable that, whereas the secant approximation stops at $SZA = 90°$, the Fitzmaurice formula (especially for higher altitudes) returns values for the ionospheric at $SZA > 90°$.
The results of the simulation, for three different inclinations ($i = 5°, 30°, 75°$) can be found in fig. 4.10. As expected, the frequency residuals are significantly smaller in magnitude compared to the output from the dayside case, as half of the occultation happens in the dark side (where, despite the more complex grazing function, electron density is still lower by several orders of magnitude). In fig. 4.11 the difference in frequency residuals estimation between the straight-line approximation and the "real" raypath for the three selected orbital configurations is shown. Once again, the absolute difference is rather small: in this case it is always within 3 mHz, significantly lower than the difference calculated on the sun-lit side.

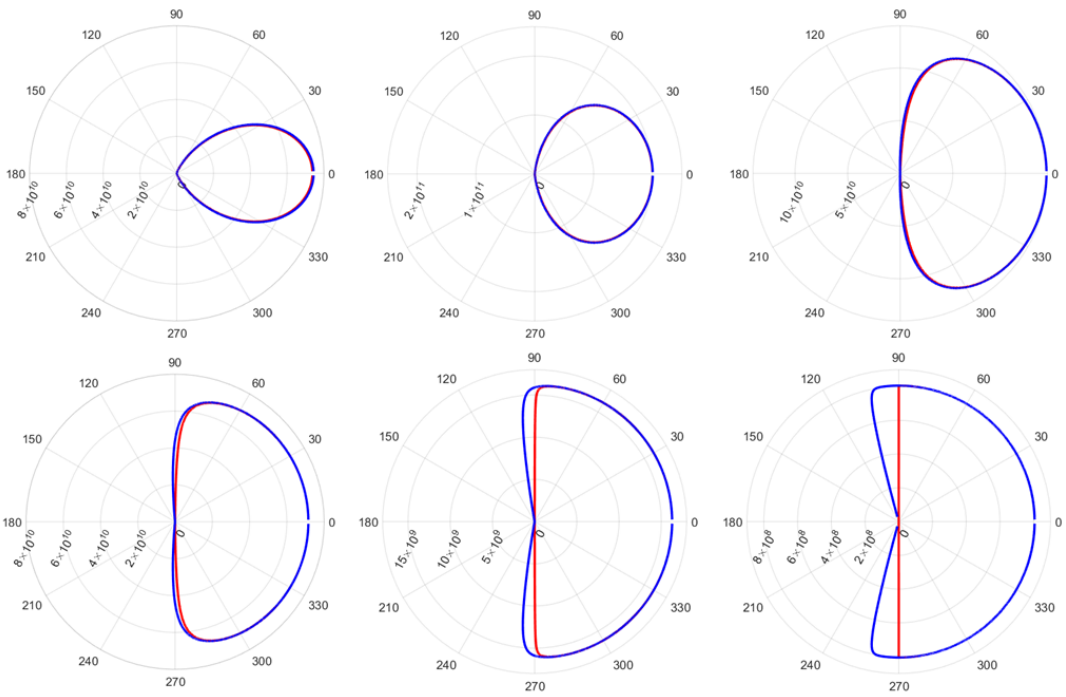

Figure 4.9: Polar plots for the equatorial electron density profiles. From top to bottom and from left to right, the altitudes are $h_m - 20$ km, h_m km, $h_m + 20$ km, $h_m + 40$ km, $h_m + 80$ km and $h_m + 160$ km, where h_m is the height of the peak electron density at the sub-solar point. In **red**, the electron density from the simplified Chapman profile, where $\sec\chi$ is used as grazing function; in **blue**, the Chapman profile with the Fitzmaurice grazing function. The Sun vector points towards the right side of the image. NOTE: the scale for the electron density is not the same for all plots

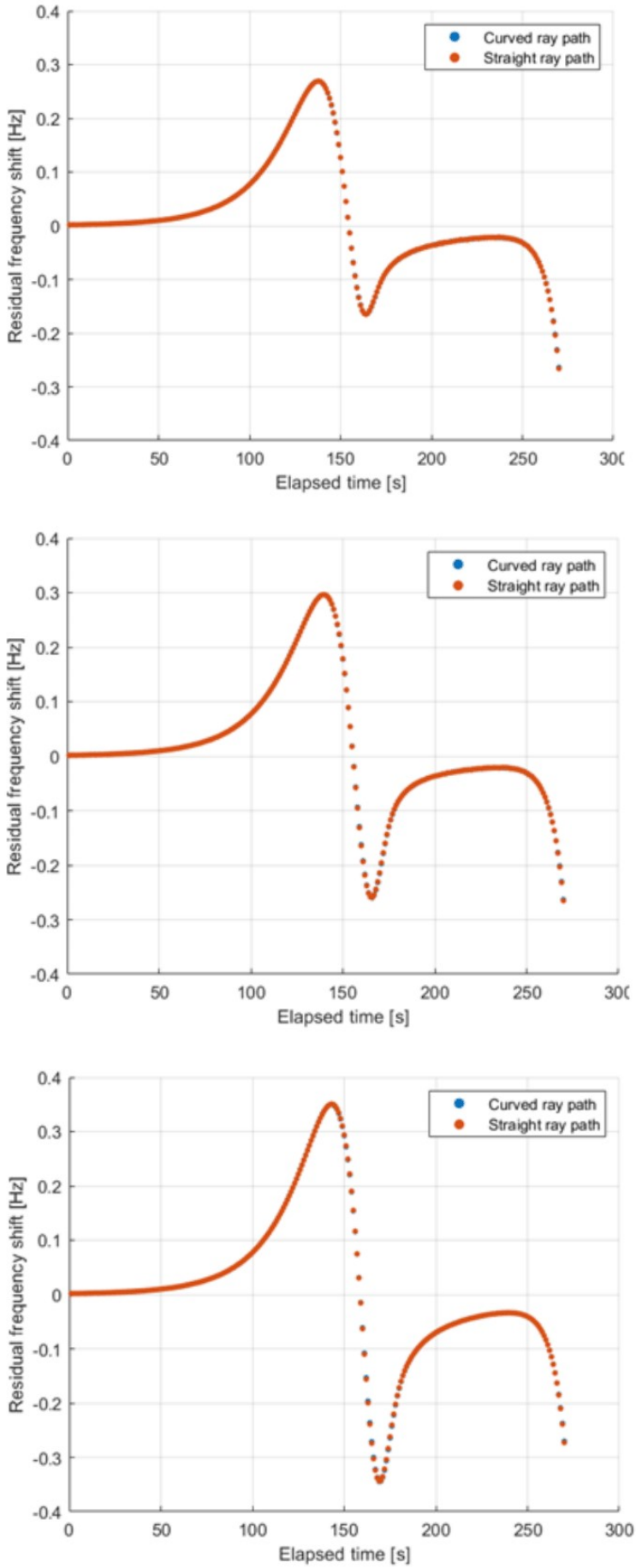

Figure 4.10: Residual frequency shift at the terminator for three different inclinations: $i = 5°$ (left), $i = 30°$ (centre), $i = 75°$ (left).

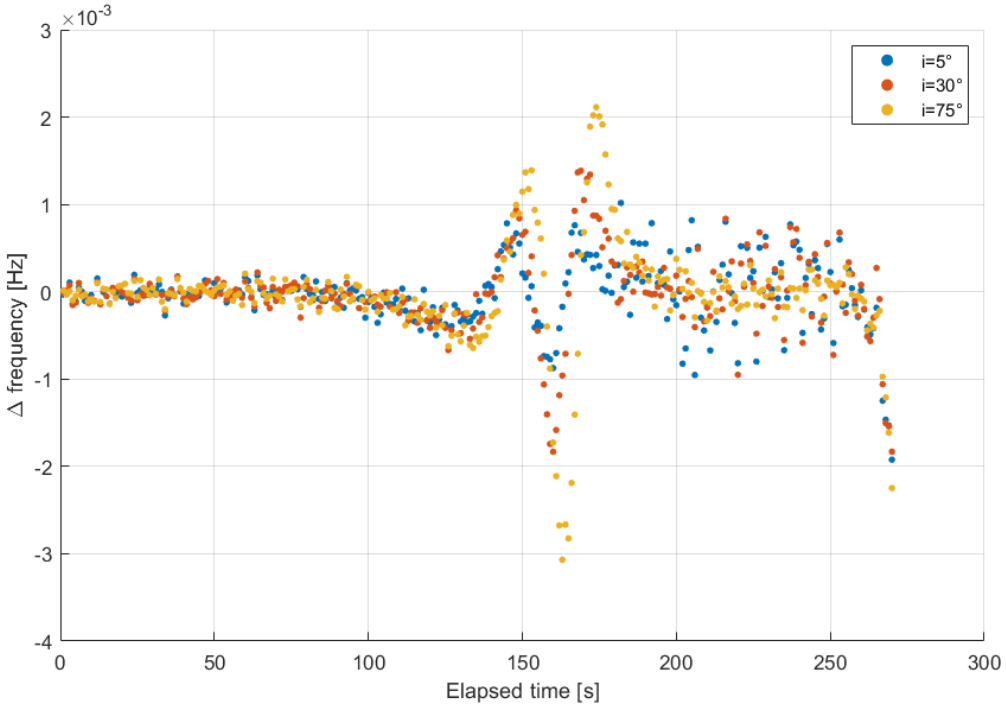

Figure 4.11: Difference between straight line and curved line approach for the terminator occultation events

5

Conclusions and further recommendations

The goal of this thesis is to provide a thorough analysis of the error introduced by calculating the frequency shift of a radio-occultation event at Mars with a ”straight line approximation”, for the purpose of using this calculation method to retrieve atmospheric parameters with the so-called ”forward propagation” optimization technique. To do so, several possible occultation scenarios have been investigated: dayside occultation (with real orbital data from MEX and TGO spacecraft) with spherical symmetry, dayside occultation with longitudinal asymmetry and terminator occultation with longitudinal asymmetry.
For the spherical symmetric case, the difference between the two methodologies has been found negligible, smaller than the measurement noise in the radio-occultation measurements performed between Mars Express and ExoMars Trace Gas Orbiter. This statement has been proved by inverting the resulting frequency residuals with the Abel transform, thus obtaining the refractivity profiles; from those profiles we can conclude that not only the absolute difference between the two approaches is small in the frequency domain, but also that the two methods lead to very similar results in the calculation of the index of refraction (and, from there, to the estimate of surface pressure and ionospheric electron content).
However, the introduction of the straight line method has been proposed to better interpret the frequency shifts coming from regions with an asymmetric distribution in atmospheric parameters, such as the terminator (the boundary between the sunlit and the night side). Restricting the analysis to the ionosphere (which is by far the larger contributor to the atmospheric effect) and introducing the so-called ”Chapman grazing function” we were able to model an electron density distribution more adherent to reality, with a continuous decrease in electron density as the solar zenith angle increases, until reaching zero *beyond* the terminator line. Under this conditions, radio-occultation measurements have been simulated at different locations (sunlit side with a high gradient in electron density, directly above the terminator line) and configurations (from equatorial to polar orbits) and the results have shown that the difference between the two methods is in the same order of magnitude as in the spherical symmetric case (even less when the occultation occurs over the terminator). Despite the fact that Abel inversion is not applicable in this case (as it only works under spherical symmetry conditions) we could expect that, by using a forward-modeling technique for the calculation of electron density, the error introduced by assuming a straight line propagation would be the same as the one obtained for the spherical symmetric case (less than 1%).
It is now possible to answer the research questions from chapter 1:

- *In the context of the study of the atmospheric effect based on residual frequency shift, how large is the difference between straight-line approximation and the ”real” frequency shift?*
  The atmospheric effect (i.e. the frequency shift that is measured in any Doppler measurement as a consequence of the passage of the radio signal through a medium) simulated for Mars is in the order of units of Hz; in the simulation that featured the most extreme conditions for Mars ionosphere, the maximum value of this effect almost reached +2 Hz. For that simulation, the difference between the two approaches never exceeded 0.07 Hz; during large part of the

occultation event ($\sim$ 88% of the total time) the difference between the two approaches never exceeded ± 0.02 Hz. This discrepancy leads to an error of 0.25% in the estimate of the ionospheric peak, and to an error of 0.50% in the estimate of bottom tropospheric pressure. For lower electron densities, the difference decreases further: when introducing spherical asymmetry, at $\chi = 60°$ almost never exceeds 0.03 Hz (being bounded within ± 0.01 Hz for ~ 85% of the total occultation event); for occultations over the terminator line, the difference is even lower, not exceeding 0.004 Hz.

- How significant is this difference when compared to the measurement noise?
  Available data to estimate the measurement noise during a radio-occultation measurement come from a single occultation event between MEX and TGO spacecraft, which we consider to be representative for the average communication link performance: any general conclusion therefore only regards the MEX-TGO link. While the largest error introduced by the straight-line approximation was of ≈ 0.07 Hz (in the worst-case scenario of sub-solar point occultation, perihelion and high solar activity), the measurement noise was estimated to be ≈ 0.09 Hz. Therefore, the error introduced by the straight-line approximation has been found to *always* be smaller than the measurement noise.
- *What are the main differences in the atmospheric effect estimation based on two-satellites occultation events for Mars and Earth?*
  Earth has a thicker and denser atmosphere when compared to Mars: the pressure at the surface is higher by a factor >100, while the ionospheric peak is at least 10 times more dense in terms of free electron content; moreover, these regions occupy a larger space, given the relative dimensions (and the scale heights) of the two planets. Consequently, the atmospheric effect has a larger magnitude, almost reaching 20 Hz for the ionospheric effect. However, despite the differences in magnitude, the straight-line approach proved to be applicable for the study of Earth ionosphere as well, returning an error in the estimate of the peak electron density comparable to the Mars case (~ 0.28%); on the other hand, this approximation fails when trying to transform the tropospheric effect into a refractivity profile. This is a first estimation based on spherical symmetry assumption, which particularly on Earth is quite unrealistic (due to a stratified, complex ionosphere that interacts with the magnetosphere, generating local, non radially-symmetrical phenomena such as the equatorial electron jets).

The present work could be further expanded by elaborating a comprehensive description of the *forward propagation* (the technique mentioned in section 1.2 as complementary to the straight line approximation). Some key features of the algorithm shown in fig. 1.6 that need a proper definition include:

- The type of model that can be built, and the number of independent parameters it can contain. It has been shown in section 3.2 that the relatively small number of observations puts a limit to the complexity of the model one might decide to use. One solution, following the example of Howe, Runciman, and Secan 1998, might be reducing the number of parameters by approximating the electron density and the atmospheric pressure-over-temperature ratio functions as a finite sum of *spherical harmonics* in the horizontal direction and of *empirical orthogonal functions* in the vertical direction. In any case, the limited amount of frequency measurements during an occultation event must be taken into account when designing the atmospheric model
- The iterative method used to estimate the atmospheric parameters. This is where optimization theory must be used, as the are facing a multi-variable, non-linear optimization problem
- Solvability of the problem. Depending on the model adopted, there might be a manifold of solutions that approximate with the same degree of confidence the observed data: this must be established before proceeding with the calculations
- Validation of the forward propagation method. A profitable test bed for the development of such method would be the Earth ionosphere. It has been proved that the straight line approach doesn't introduce a large error, and the amount of data available is vast and covers an extended period of time, including periodic variations such as seasons and solar activity cycles; IRI database would probably be the best benchmark to test the validity of ionospheric modeling with forward propagation.

In conclusion, the first tool (the straight-line approximation) of this new method for atmospheric parameter estimation (for which there is no mention in the literature dedicated to planetary radio-occultation measurements) has been proven to be valid and usable in different context. If the method as a whole works, radio occultation measurements might be used to detect horizontal variations in atmospheric parameters; realistically, the field of investigation would probably be restricted to ionospheric variables, as the lower neutral layers, due to geometry constraints, are usually sampled for a much shorter time.

References

Acuña, M. H. et al. (Mar. 1998). “Magnetic Field and Plasma Observations at Mars: Initial Results of the Mars Global Surveyor Mission”. In: *Science* 279.5357, pp. 1676–1680. ISSN: 0036-8075. DOI: 10.1126/science.279.5357.1676.

Ao, C. O. et al. (Oct. 2015). “A first demonstration of Mars crosslink occultation measurements”. In: *Radio Science* 50.10, pp. 997–1007. ISSN: 1944799X. DOI: 10.1002/2015RS005750.

Bennett, J. A., P. L. Dyson, and R. J. Norman (2004). “Progress in radio ray tracing in the ionosphere”. In: *URSI Radio Science Bulletin* 2004.310, pp. 81–91.

Bilitza, Dieter (Sept. 2018). “IRI the international standard for the ionosphere”. In: *Advances in Radio Science* 16, pp. 1–11. ISSN: 16849973. DOI: 10.5194/ars-16-1-2018.

Born, Max and Emil Wolf (1959). *Principles of Optics*. Pergamon Press. ISBN: 978-1-108-47743-7.

CCSDS (July 2006). *PROXIMITY-1 SPACE LINK PROTOCOL— DATA LINK LAYER*. Tech. rep. CCSDS.

Chapman, Sydney (1931). “The absorption and dissociative or ionizing effect of monochromatic radiation in an atmosphere on a rotating Earth”. In: *Proceedings of the Physical Society* 43.26, pp. 26–45.

Coleman, Christopher J. (Oct. 2011). “Point-to-point ionospheric ray tracing by a direct variational method”. In: *Radio Science* 46.5, n/a–n/a. ISSN: 00486604. DOI: 10.1029/2011RS004748.

Edwards, Charles D. et al. (2003). “The Electra proximity link payload for Mars relay telecommunications and navigation”. In.

Fehmers, G. C. (1996). “Tomography of the ionosphere”. PhD thesis. Eindhoven: Eindhoven University of Technology.

Fischbach, Frederick F (1965). “A satellite method for pressure and temperature below 24 km”. In: *Bulletin American Meteorological Society* 49.9, pp. 528–532.

Fitzmaurice, John A. (May 1964). “Simplification of the Chapman Function for Atmospheric Attenuation”. In: *Applied Optics* 3.5. ISSN: 0003-6935. DOI: 10.1364/AO.3.000640.

Fjeldbo, G. et al. (1975). “The Pioneer 10 Radio Occultation Measurements of the Ionosphere of Jupiter”. In: *Astronomy & Astrophysics* 39, pp. 91–96.

Fjeldbo, Gunnar, Arvydas J Kliore, and R Eshleman (1971). “The Neutral Atmosphere of Venus as Studied with the Mariner V Radio Occultation Experiments”. In: *The Astronomical Journal* 76.2.

Formisano, Vittorio et al. (Dec. 2004). “Detection of Methane in the Atmosphere of Mars”. In: *Science* 306.5702. ISSN: 0036-8075. DOI: 10.1126/science.1101732.

Gladstone, G. Randall et al. (Mar. 2016). “The atmosphere of Pluto as observed by New Horizons”. In: *Science* 351.6279. ISSN: 0036-8075. DOI: 10.1126/science.aad8866.

Gómez-Correa, J. E. et al. (Oct. 2021). “Generalization of ray tracing in symmetric gradient-index media by Fermat’s ray invariants”. In: *Optics Express* 29.21. ISSN: 1094-4087. DOI: 10.1364/OE.440410.

Hargreaves, John Keith (Aug. 1992). *The Solar-Terrestrial Environment*. Cambridge University Press. ISBN: 9780521427371. DOI: 10.1017/CBO9780511628924.

Harri, Ari-Matti et al. (Oct. 2006). “Vertical pressure profile of Titan—observations of the PPI/HASI instrument”. In: *Planetary and Space Science* 54.12. ISSN: 00320633. DOI: 10.1016/j.pss.2006.05.037.

Haselgrove, C B and Jenifer Haselgrove (Mar. 1960). “Twisted Ray Paths in the Ionosphere”. In: *Proceedings of the Physical Society* 75.3, pp. 357–363. ISSN: 0370-1328. DOI: 10.1088/0370-1328/75/3/304.

Haselgrove, J. (1955). *Ray Theory and a New Method for Ray Tracing*. Tech. rep. London: Physical Society of London.

Haselgrove, Jenifer (July 1963). “The Hamiltonian ray path equations”. In: *Journal of Atmospheric and Terrestrial Physics* 25.7, pp. 397–399. ISSN: 00219169. DOI: 10.1016/0021-9169(63)90173-9.

Hernández-Pajares, Manuel et al. (Dec. 2011). “The ionosphere: Effects, GPS modeling and the benefits for space geodetic techniques”. In: *Journal of Geodesy* 85.12, pp. 887–907. ISSN: 09497714. DOI: 10.1007/s00190-011-0508-5.

Hinson, D. P. et al. (Nov. 1999). “Initial results from radio occultation measurements with Mars Global Surveyor”. In: *Journal of Geophysical Research: Planets* 104.E11. ISSN: 01480227. DOI: 10.1029/1999JE001069.

Ho, Christian, Nasser Golshan, and Arvydas Kliore (2002). *Radio Wave Propagation Handbook for Communication on and Around Mars*. Tech. rep.

Howe, Bruce M., Kay Runciman, and James A. Secan (Jan. 1998). “Tomography of the ionosphere: Four-dimensional simulations”. In: *Radio Science* 33.1, pp. 109–128. ISSN: 00486604. DOI: 10.1029/97RS02615.

Kliore, A. J. et al. (Jan. 1972). “Mariner 9 S-Band Martian Occultation Experiment: Initial Results on the Atmosphere and Topography of Mars”. In: *Science* 175.4019. ISSN: 0036-8075. DOI: 10.1126/science.175.4019.313.

Kliore, Arvydas, Dan L. Cain, et al. (Sept. 1965). “Occultation Experiment: Results of the First Direct Measurement of Mars’s Atmosphere and Ionosphere”. In: *Science* 149.3689. ISSN: 0036-8075. DOI: 10.1126/science.149.3689.1243.

Kliore, Arvydas, Gunnar Fjeldbo, et al. (Dec. 1969). “Mariners 6 and 7: Radio Occultation Measurements of the Atmosphere of Mars”. In: *Science* 166.3911. ISSN: 0036-8075. DOI: 10.1126/science.166.3911.1393.

Kliore, Arvydas J. et al. (1980). “Structure of the ionosphere and atmosphere of Saturn From Pioneer 11 Saturn radio occultation”. In: *Journal of Geophysical Research* 85.A11, pp. 5857–5870. ISSN: 0148-0227. DOI: 10.1029/JA085iA11p05857.

Knudsen, William C. et al. (Aug. 2016). “Measurement of solar wind electron density and temperature in the shocked region of Venus and the density and temperature of photoelectrons within the ionosphere of Venus”. In: *Journal of Geophysical Research: Space Physics* 121.8. ISSN: 2169-9380. DOI: 10.1002/2016JA022526.

Kolosov, M. A. et al. (1972). “Preliminary results of the Martian atmosphere investigation by means of the “Mars-2” satellite”. In: *Proceedings of the USSR Academy of Sciences* 206.5, pp. 1071–1073.

Kursinski, E. R. et al. (Oct. 1997). “Observing Earth’s atmosphere with radio occultation measurements using the global positioning system”. In: *Journal of Geophysical Research Atmospheres* 102.19, pp. 23429–23465. ISSN: 01480227. DOI: 10.1029/97jd01569.

Lindal, G F et al. (1983). “The Atmosphere of Titan: An Analysis of the Voyager 1 Radio Occultation Measurements 1”. In: *Icarus* 53, pp. 348–363.

Lindal, Gunnar F. (1992). “The atmosphere of Neptune: an analysis of radio occultation data acquired with Voyager 2”. In: *The Astronomical Journal* 103.3, pp. 967–982.

Lindal, Gunnar F. et al. (1979). “Viking radio occultation measurements of the atmosphere and topography of Mars: Data acquired during 1 Martian year of tracking”. In: *Journal of Geophysical Research* 84.B14. ISSN: 0148-0227. DOI: 10.1029/JB084iB14p08443.

Lusignan, Bruce et al. (1969). “Sensing the Earth’s Atmosphere with Occultation Satellites”. In: *Proceedings of the IEEE* 57.4, pp. 458–467. ISSN: 15582256. DOI: 10.1109/PROC.1969.7000.

Melbourne, William G. (2004). *Radio Occultations Using Earth Satellites: A Wave Theory Treatment*. Ed. by Joseph H. Yuen. Wiley.

Mumma, Michael J. et al. (Feb. 2009). “Strong Release of Methane on Mars in Northern Summer 2003”. In: *Science* 323.5917. ISSN: 0036-8075. DOI: 10.1126/science.1165243.

NAIF (2021). *https://naif.jpl.nasa.gov/naif/*.

Nava, B et al. (2020). *Mutual Occultation Experiment between the Trace Gas Orbiter and Mars Express (ROMA)*. Tech. rep.

Němec, F., D. J. Andrews, et al. (May 2019). “Oblique Reflections of Mars Express MARSIS Radar Signals From Ionospheric Density Structures: Raytracing Analysis”. In: *Journal of Geophysical Research: Planets*, 2018JE005891. ISSN: 2169-9097. DOI: 10.1029/2018JE005891.

Němec, F., D. D. Morgan, et al. (July 2011). “Dayside ionosphere of Mars: Empirical model based on data from the MARSIS instrument”. In: *Journal of Geophysical Research* 116.E7. ISSN: 0148-0227. DOI: 10.1029/2010JE003789.

Nickisch, L. J. (2008). “Practical applications of Haselgrove’s equations for HF systems”. In: *URSI Radio Science Bulletin* 2008.325, pp. 36–48.

Ortiz, J. L. et al. (Nov. 2012). “Albedo and atmospheric constraints of dwarf planet Makemake from a stellar occultation”. In: *Nature* 491.7425. ISSN: 0028-0836. DOI: 10.1038/nature11597.

Pi, Xiaoqing et al. (2008). *A Chapman-Layers Ionospheric Model for Mars*. Tech. rep.

Reboud, O., M. Denis, and T. Ormston (2012). *Mars Express and the NASA landers and rovers on Mars - Sustaining a backup relay in an interplanetary network*. Tech. rep. American Institute of Aeronautics and Astronautics.

Reilly, Michael H. (July 1991). "Upgrades for efficient three-dimensional ionospheric ray tracing: Investigation of HF near vertical incidence sky wave effects". In: *Radio Science* 26.4, pp. 971–980. ISSN: 00486604. DOI: 10.1029/91RS00582.

Riedler, W. et al. (Oct. 1989). "Magnetic fields near Mars: first results". In: *Nature* 341.6243, pp. 604–607. ISSN: 0028-0836. DOI: 10.1038/341604a0.

Sánchez-Cano, B et al. (2010). *Study of the ionosphere of Mars: application and limitations of the Chapman-layer model*. Tech. rep.

Sánchez-Cano, B. et al. (July 2013). "NeMars: An empirical model of the martian dayside ionosphere based on Mars Express MARSIS data". In: *Icarus* 225.1, pp. 236–247. ISSN: 00191035. DOI: 10.1016/j.icarus.2013.03.021.

Sauer, Timothy (2011). *Numerical Analysis*. 2nd. Pearson.

Schreiner, William S. et al. (July 1999). "Analysis and validation of GPS/MET radio occultation data in the ionosphere". In: *Radio Science* 34.4, pp. 949–966. ISSN: 00486604. DOI: 10.1029/1999RS900034.

Schunk, Robert W. and Andrew F. Nagy (June 2000). "Ionospheric Measurement Techniques". In: *Ionospheres*. Cambridge University Press. DOI: 10.1017/CBO9780511551772.014.

Seidelmann, P. K. and T. Fukushima (Nov. 1992). "Why new time scales?" In: *Astronomy and Astrophysics* 265, pp. 833–838.

Shaikh, M. M., R. Notarpietro, and B. Nava (Feb. 2014). "The impact of spherical symmetry assumption on radio occultation data inversion in the ionosphere: An assessment study". In: *Advances in Space Research* 53.4, pp. 599–608. ISSN: 02731177. DOI: 10.1016/j.asr.2013.10.025.

Sharma, Anurag, D. Vizia Kumar, and A. K. Ghatak (Mar. 1982). "Tracing rays through graded-index media: a new method". In: *Applied Optics* 21.6. ISSN: 0003-6935. DOI: 10.1364/AO.21.000984.

Sicardy, B. et al. (Oct. 2011). "A Pluto-like radius and a high albedo for the dwarf planet Eris from an occultation". In: *Nature* 478.7370. ISSN: 0028-0836. DOI: 10.1038/nature10550.

Smith, Edward J. et al. (Sept. 1965). "Magnetic Field Measurements near Mars". In: *Science* 149.3689, pp. 1241–1242. ISSN: 0036-8075. DOI: 10.1126/science.149.3689.1241.

Smith, Michael D. (2008). "Spacecraft observations of the Martian atmosphere". In: *Annual Review of Earth and Planetary Sciences* 36, pp. 191–219. ISSN: 00846597. DOI: 10.1146/annurev.earth.36.031207.124334.

Strangeways, Hal J. (Oct. 2000). "Effect of horizontal gradients on ionospherically reflected or transionospheric paths using a precise homing-in method". In: *Journal of Atmospheric and Solar-Terrestrial Physics* 62.15, pp. 1361–1376. ISSN: 13646826. DOI: 10.1016/S1364-6826(00)00150-4.

Svedhem, Håkan (Sept. 2020). *MEX-TGO Mutual Occultation experiment description*. Tech. rep. European Space Agency.

— (2022). *(private communication)*.

Svedhem, Håkan et al. (Sept. 2021). *First results from the MEX – TGO Mutual Radio Occultation Experiment*.

Teunissen, Peter J.G. and Oliver Montenbruck (2017). "Springer Handbook of Global Navigation Satellite Systems-Springer". In: Springer, pp. 184–189.

Tyler, G. L. et al. (July 1986). "Voyager 2 Radio Science Observations of the Uranian System: Atmosphere, Rings, and Satellites". In: *Science* 233, pp. 79–84.

United States Committee on Extension to the Standard Atmosphere (1976). *U.S. standard atmosphere, 1976*. Washington.

Vasylyev, Dmytro (Dec. 2021). "Accurate analytic approximation for the Chapman grazing incidence function". In: *Earth, Planets and Space* 73.1. ISSN: 1880-5981. DOI: 10.1186/s40623-021-01435-y.

Webster, Guy, Dwayne Brown, and Laurie Cantillo (2016). *Europe's New Mars Mission Bringing NASA Radios Along*.

Zhang, Qingpeng et al. (Jan. 2021). "Ray Tracing Method of Gradient Refractive Index Medium Based on Refractive Index Step". In: *Applied Sciences* 11.3. ISSN: 2076-3417. DOI: 10.3390/app11030912.